Supporting Information

Achieving superior oxygen evolution of perovskite via phase transition and electrochemical reconstruction strategy

Yi-ru Hao[1,†], Hui Xue[1,†], Jing Sun[1], Niankun Guo[1], Tianshan Song[1], Hongliang Dong[5], Zhonglong Zhao[3,*], Jiangwei Zhang[2,*], Limin Wu[2,4*], and Qin Wang[1,2,*]

[1]College of Chemistry and Chemical Engineering, Inner Mongolia University, Hohhot 010021, China
[2]College of Energy Materials and Chemistry, Inner Mongolia University, Hohhot 010021, China
[3]School of Physical Science and Technology, Inner Mongolia University, Hohhot 010021, China
[4]Department of Materials Science and State Key Laboratory of Molecular Engineering of Polymers, Fudan University, Shanghai 200433, China
[5]Center for High Pressure Science and Technology Advanced Research, Shanghai 201203, China
*Email for Correspondence: qinwang@imu.edu.cn, zjw11@tsinghua.org.cn, zlzhao@imu.edu.cn, lmw@fudan.edu.cn
† These authors contributed equally to this work.

Experimental section

Method and Materials

All reagents used were not further purified. $Co(NO_3)_2 \cdot 6H_2O$ (99%, AR), $Sr(NO_3)_2$ (99%, AR), and $C_6H_8O_7 \cdot H_2O$ (99%, AR) obtained from Tianjin Fengchuan Chemical Reagent Technology Co., Ltd. $RuCl_3 \cdot xH_2O$ and Nafion® per-fluorinated resin solution was bought from Adamas-beta®.

Synthesis of Ru-Co_3O_4-x

5, 10, and 20 mL of $RuCl_3 \cdot xH_2O$ were introduced to synthesize Ru-Co_3O_4-x (x=5, 10, and 20), respectively.

Materials characterization:

XRD was characterized in a PuXi XD3 diffractometer. XPS was measured on a VG Scientific ESCALAB Mark II spectrometer. SEM pictures of the catalyst were recorded on a JEOL-JSM 6700-F. JEM-ARM 300F GRAND ARM, JEM-2100F, and HITACHI 800 were used to obtain TEM images, HR-TEM images, and STEM elemental mapping images of various catalysts.

Shirley background correction was used to calculate all spectra in the center of the d-band. The formula for calculating the d-band center of different catalysts is:

$$\varepsilon_d = \frac{\int \mathrm{N}(\varepsilon)\varepsilon d\varepsilon}{\int \mathrm{N}(\varepsilon) d\varepsilon} \qquad (1)$$

which range from -∞ to +∞, ε is energy, $N(\varepsilon)$ is the density of states.

XAFS measurements:

The X-ray absorption find structure spectra Ru K-edge were collected at BL14W1 beamline of Shanghai Synchrotron Radiation Facility (SSRF) while Co K-edge were collected at BL17B beamline of National Facility for Protein Science (NFPS), Shanghai Synchrotron Radiation Facility (SSRF) Shanghai, China. The data were collected in transmission mode or fluorescence

mode using a Lytle detector while the corresponding reference sample were collected in transmission mode. while the corresponding oxyde reference sample were collected in transmission mode in TableXAFS-500A from Anhui Chuangpu Instrument Technology Co.,LTD. The sample were grinded and uniformly daubed on the special adhesive tape. In-situ XAFS was collected at in-situ three-electrode cell.

XAFS Analysis and Results:

The acquired EXAFS data were processed according to the standard procedures using the ATHENA module of Demeter software packages.

The EXAFS spectra were obtained by subtracting the post-edge background from the overall absorption and then normalizing with respect to the edge-jump step. Subsequently, the χ(k) data of were Fourier transformed to real (R) space using a hanning windows (dk=1.0 $Å^{-1}$) to separate the EXAFS contributions from different coordination shells. To obtain the quantitative structural parameters around central atoms, least-squares curve parameter fitting was performed using the ARTEMIS module of Demeter software packages

The following EXAFS equation was used:

$$\chi(k) = \sum_j \frac{N_j S_0^2 F_j(k)}{kR_j^2} \cdot \exp[-2k^2\sigma_j^2] \cdot \exp[\frac{-2R_j}{\lambda(k)}] \cdot \sin[2kR_j + \phi_j(k)]$$

the theoretical scattering amplitudes, phase shifts and the photoelectron mean free path for all paths calculated. S_0^2 is the amplitude reduction factor, $F_j(k)$ is the effective curved-wave backscattering amplitude, N_j is the number of neighbors in the jth atomic shell, R_j is the distance between the Xray absorbing central atom and the atoms in the jth atomic shell (backscatterer), λ is the mean free path in Å, $\phi_j(k)$ is the phase shift (including the phase shift for each shell and the total central atom phase shift), σ_j is the Debye-Waller parameter of the jth atomic shell

(variation of distances around the average R_j). The functions $F_j(k)$, λ and $\phi_j(k)$ were calculated with the ab initio code FEFF10. The additional details for EXAFS simulations are given below. All fits were performed in the *R* space with *k*-weight of 2 while phase correction was also applied in the first coordination shell to make R value close to the physical interatomic distance between the absorber and shell scatterer. The coordination numbers of model samples were fixed as the nominal values. While the S_0^2, internal atomic distances R, Debye-Waller factor σ^2, and the edge-energy shift Δ were allowed to run freely.

Pair Distribution Function (PDF) Measurements and Analysis:

X-ray total scattering data were measured at BL17b beamline in energy state of 20 keV (0.6199 Å) of National Facility for Protein Science (NFPS), Shanghai Synchrotron Radiation Facility (SSRF). The 2D XRD image was first integrated to obtain 1D total scattering intensity I(Q) calibration by CeO_2 calibrant by Dioptas0.5.2 package. Additional scattering measurements from kapton capillary were performed in the same conditions for background subtraction. Then the background subtracted I(Q) was applied for the structure Rietveld refinement conducted by the program of Fullprof program and the reduced pair distribution function G(r) was obtained through Fourier transform total scattering structure function S(Q) derivate from I(Q) by PDFgetX3.

The following G(r) equation was used:

$$\mathrm{G}(r) = \frac{2}{\pi}\int_0^{\infty} Q[S(Q) - 1]\sin(Qr)dQ$$

The PDF Rietveld refinement was conducted by PDFgui. The initial structural model were built based on EXAFS fitting structural model. The following parameters including the scale factor, the cell parameters, the atomic positions except particular positions, the isotropic atomic

displacement parameters(Biso), and the dynamic correlation factor (delta2) were refined during the PDF Rietveld refinement.

The XRD Rietveld refinement was conducted by Fullprof. The initial structural model were built based on ICSD database structural model. The following parameters including the scale factor, the cell parameters, the atomic positions except particular positions, the isotropic atomic displacement parameters(Biso), and the dynamic correlation factor (delta2) were refined during the XRD Rietveld refinement.

Electrochemical tests

Perform all electrochemical measurements in the CHI 760E electrochemical workstation using a three-electrode configuration. Use a glassy carbon electrode (0.0707 cm^{-2}), carbon rod, and Hg/HgO electrode as the working electrode, the counter electrode, and reference electrode, respectively. Typical catalyst inks were prepared by disperses of 10 mg catalyst in 30 μL of 0.05% Nafion® solution, 600 μL of H_2O, and 200 μL of C_2H_5OH, and then sonicated for 0.5 h. Then apply 8 μL of ink on the working electrode. The Ru_{SA}-Co_3O_4/CoOOH catalyst was loaded on clean carbon fiber paper and used as the working electrode for chronopotentiometric stability test at 10 $mA{\cdot}cm^{-2}$. Perform OER and related tests in 1.0 M KOH solution. Measure the LSV curve at a scan rate of 10 $mV{\cdot}s^{-1}$. EIS measurement of the catalyst was performed at 0.36 V from 100 kHz to 100 MHz. CV was used to measure the double-layer capacitance (C_{dl}) of the catalyst at different scan rates in the non-Faraday zone. A constant current chronoamperometric test was performed on the catalyst to evaluate the OER stability of the catalyst.

Measurement and calculation of Faraday efficiency.

The Faraday efficiency is measured by the water-gas displacement method, and the theoretical amount of O_2 precipitation can be calculated by Faraday's law and the I-t curve. It takes four

electrons to release an oxygen molecule in an alkaline solution. The Faraday efficiency can be calculated by the following formula:

$$FE = 4F \times \frac{n_{O_2}}{Q}$$

$$= 4F \times n_{O_2} \times 10/t \qquad (2)$$

Where t is the time of constant oxidation current (s), F is the Faraday constant, and the amount of charge Q=t*0.1 (C).

Calculation of TOF.

TOF is calculated by the equation:

$$\mathrm{TOF} = \frac{\mathrm{jS}}{4\mathrm{Fn}} \qquad (3)$$

Where j is the current density at an overpotential of 300 mV; S (0.0707 cm^{-2}) is the surface area of the electrode; F is Faraday constant (96485.3 $C \cdot mol^{-1}$), and n is the moles of the total active metal atoms drop-cast on the electrode. All metals in each catalyst are assumed to be active metals.

DFT computational details.

The Vienna *ab initio* Simulation Package (VASP) with the projector-augmented wave (PAW) pseudopotentials are used to calculate the DFT.[1, 2] The exchange-correlation interaction is described by Perdew-Burke-Ernzerhof (PBE) functional.[3, 4] The plane-wave energy cutoff was taken as 400 eV and the Brillouin zone was sampled with a 3×3×1 k-point mesh according to the Monkhorst-Pack scheme.[5] The Ru-Co_3O_4 slab model was constructed based on the (110) surface of a single-crystalline spinel-type Co_3O_4 structure. In the normal direction, 15 Å vacuum separates the adjacent plates. Similar to previous studies, it is the contribution of zero energy, entropy and solvent correction to the free energy of reaction intermediate.[6] The free energy change of each reaction step is calculated by using the computational hydrogen electrode (CHE)

model.[7] In particular, in the CHE model, the free energy of an electron-proton pair is computed as half of the free energy of H_2 molecule at the standard conditions, which is then shifted by -eU upon an applied external potential U.

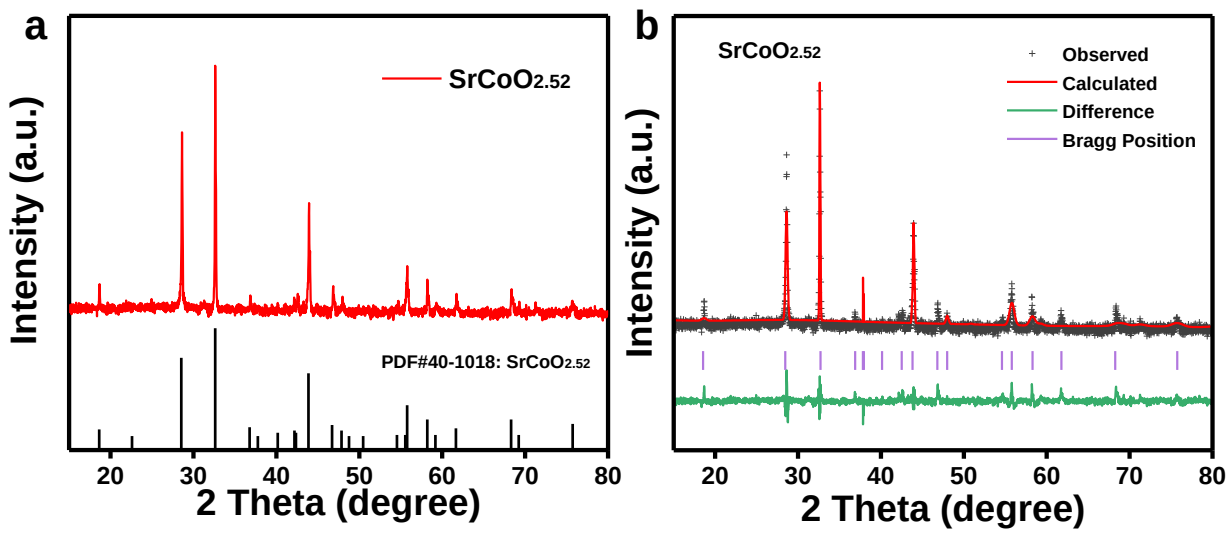

Figure S1. (a) XRD pattern of $SrCoO_{2.52}$. (b) Rietveld refined XRD patterns of $SrCoO_{2.52}$.

The XRD results of $SrCoO_{2.52}$ were further studied by Rietveld refinement (Figure S1b). All *R*-factors (R_{wp} and R_p) and χ^2 values for Rietveld refinement are low enough to indicate high reliability of the refinement data. In this work, the synthesized $SrCoO_{2.52}$ is a cubic perovskite oxide with oxygen defects whose lattice parameters are a=b=c=3.8530Å，α=β=γ=90°, and V =57.2001Å^3. Therefore, $SrCoO_{2.52}$ belongs to the *P*m-3m space group.

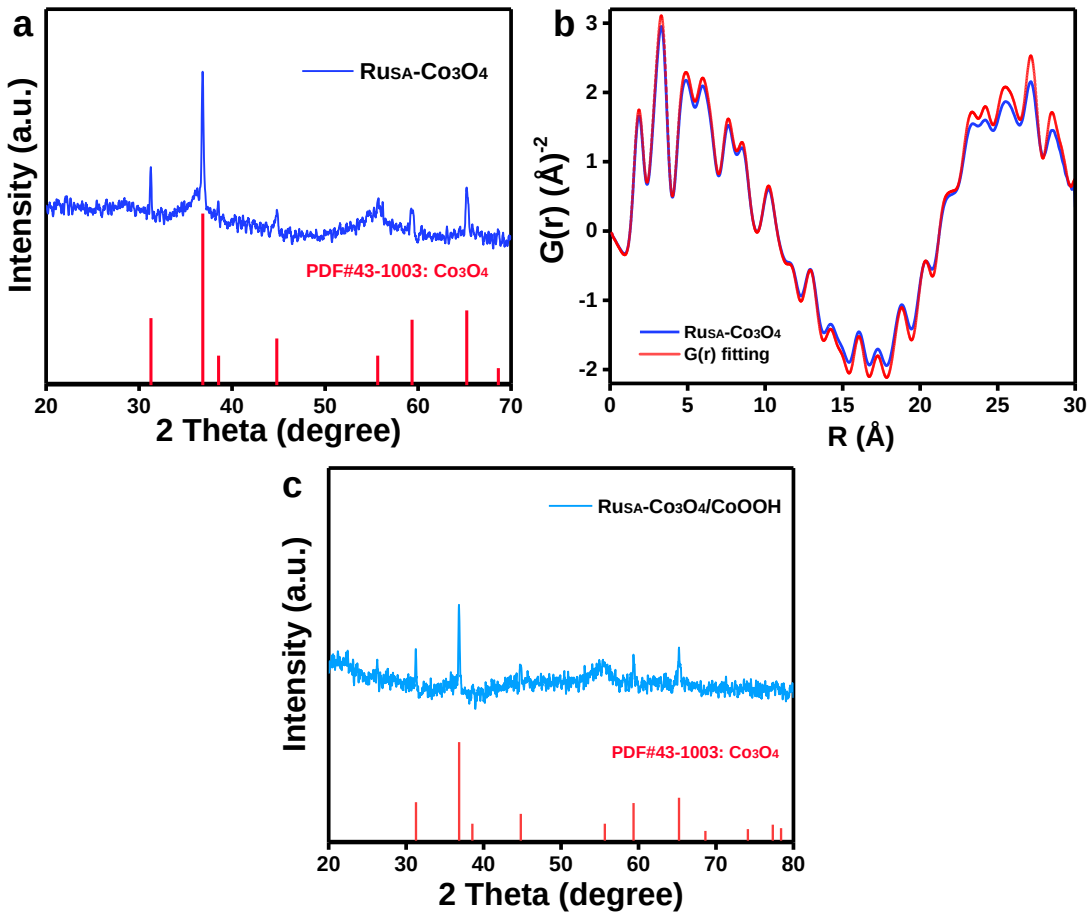

Figure S2. (a) XRD pattern of Ru_{SA}-Co_3O_4, (b) PDF Rietveld refined XRD patterns of Ru_{SA}-Co_3O_4. (c) XRD pattern of Ru_{SA}-Co_3O_4/CoOOH.

The structure of Ru_{SA}-Co_3O_4 was analyzed using real space X-ray total scattering PDF Rietveld refinement (Figure S2b). The R_w values of PDF Rietveld refinement are low enough to indicate the high reliability of the refined data. Crystal structure data from PDF Rietveld refinement for Ru_{SA}-Co_3O_4, space group *P*1 (no. 1), triclinic, a=8.0397Å, b=11.3699Å, c=21.2333Å, α=89.82°, β=91.21°, γ=91.12°, V =1940.1376 $Å^3$, χ_{sq} =301.12, Reduced χ_{sq} = 0.0633; R_w= 0.0687.

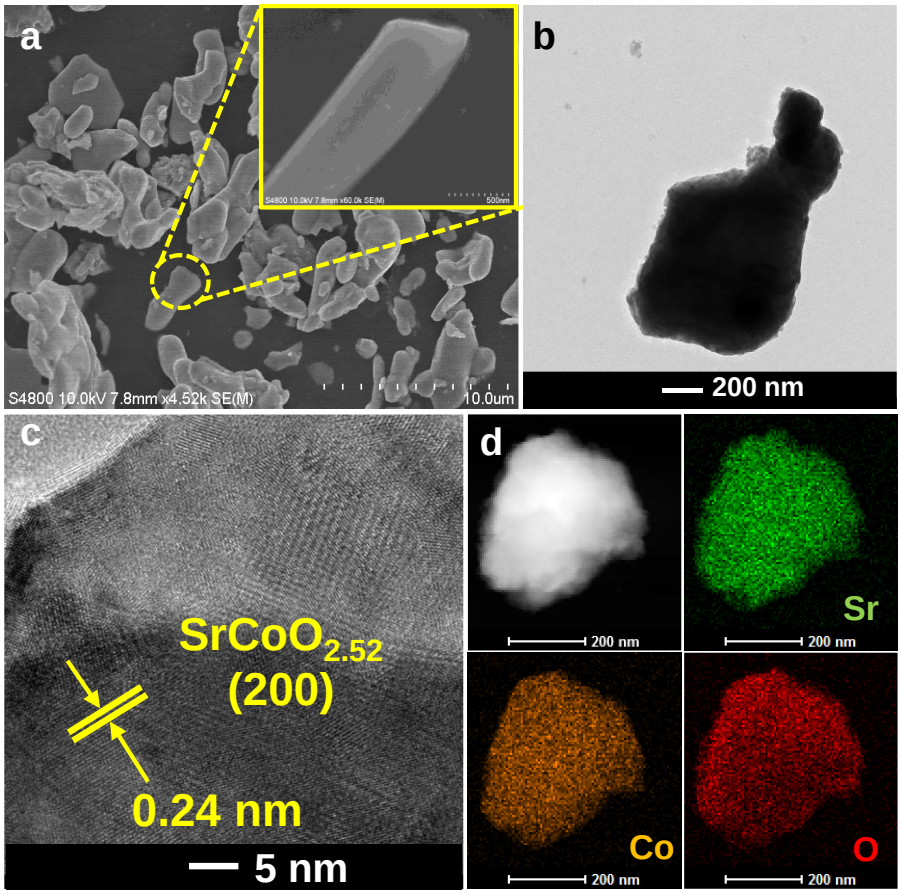

Figure S3. (a) SEM image, (b) TEM image, (c) HR-TEM, (d) element mapping of $SrCoO_{2.52}$.

The bulk $SrCoO_{2.52}$ catalyst with a smooth surface can be observed by SEM and TEM (Figure S3a, b). HR-TEM image shows a clear interplanar space of 0.24 nm (Figure S3c), which is attributed to the (200) plane of the $SrCoO_{2.52}$. The elemental mapping results of $SrCoO_{2.52}$ indicate a uniform distribution of Sr, Co, and O elements (Figure S3d).

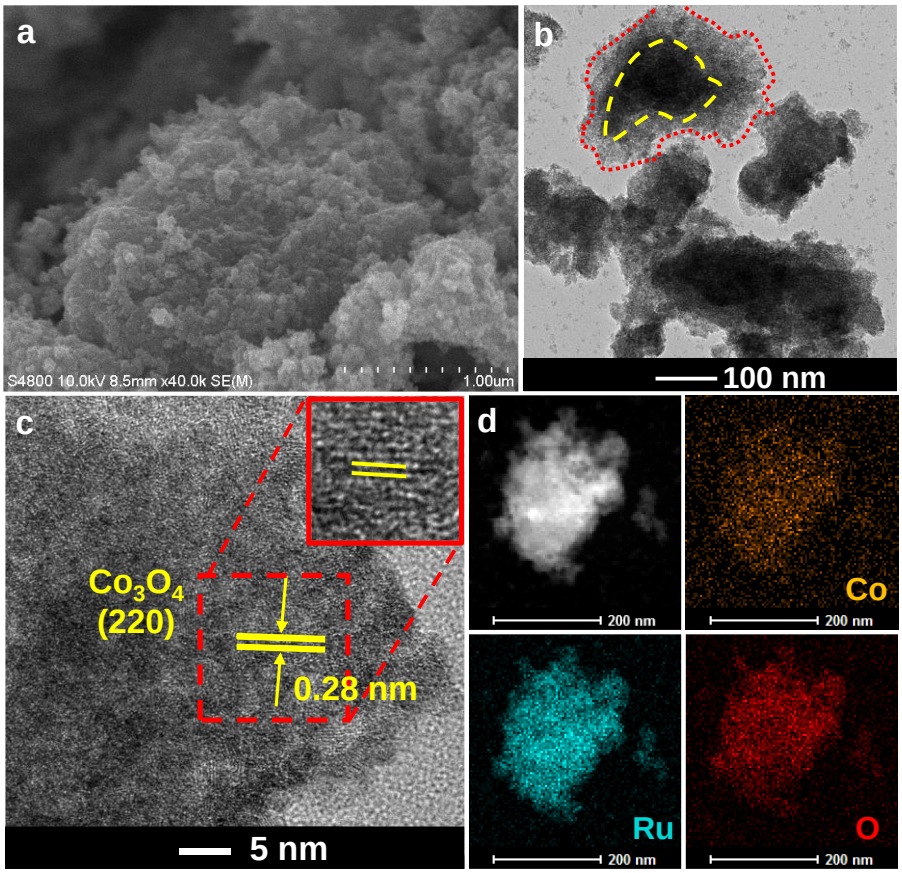

Figure S4. (a) SEM image, (b) TEM image, (c) HR-TEM image, (d) element mapping of Ru_{SA}-Co_3O_4.

Figure S4a, b show that after the introduction of $RuCl_3 \cdot xH_2O$, the crystal structure of $SrCoO_{2.52}$ is reconstructed and a large number of irregular fine particles are formed on the surface of the catalyst. The interplane spacing of 0.28 nm corresponds to the (220) facet of Co_3O_4, further confirming the transformation of $SrCoO_{2.52}$ into spinel (Figure S4c). The elemental mapping results of Ru_{SA}-Co_3O_4 indicate a uniform distribution of Ru, Co, and O elements (Figure S4d).

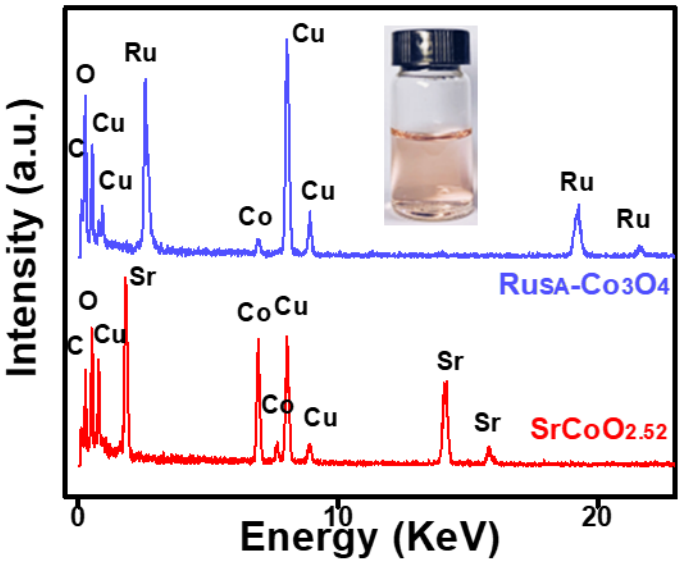

Figure S5. EDS spectra of $SrCoO_{2.52}$ and Ru_{SA}-Co_3O_4 (the inset is the collection of the centrifuge after the first reconstruction).

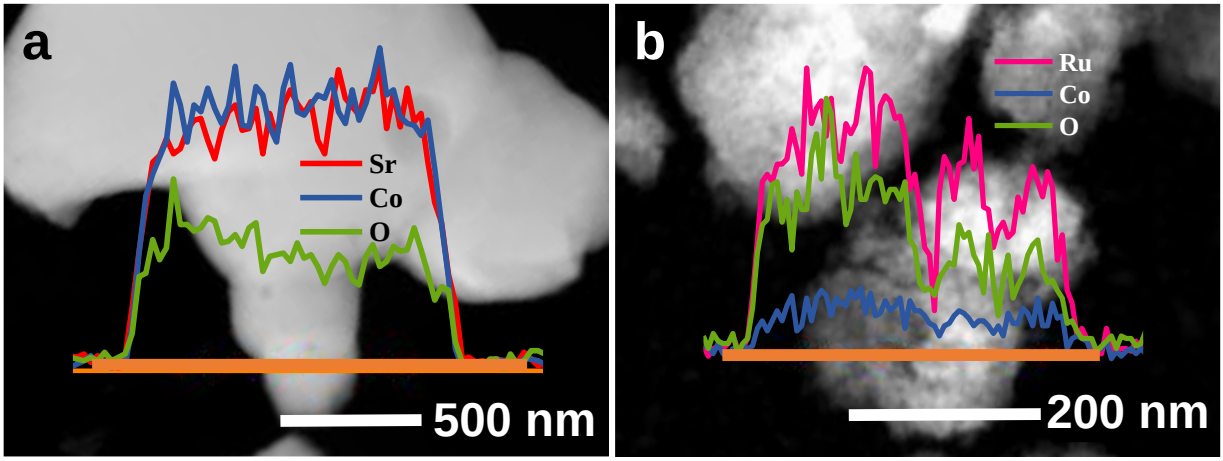

Figure S6. HAADF-STEM (inset shows the EDS line scans) of (a) $SrCoO_{2.52}$, (b) Ru_{SA}-Co_3O_4.

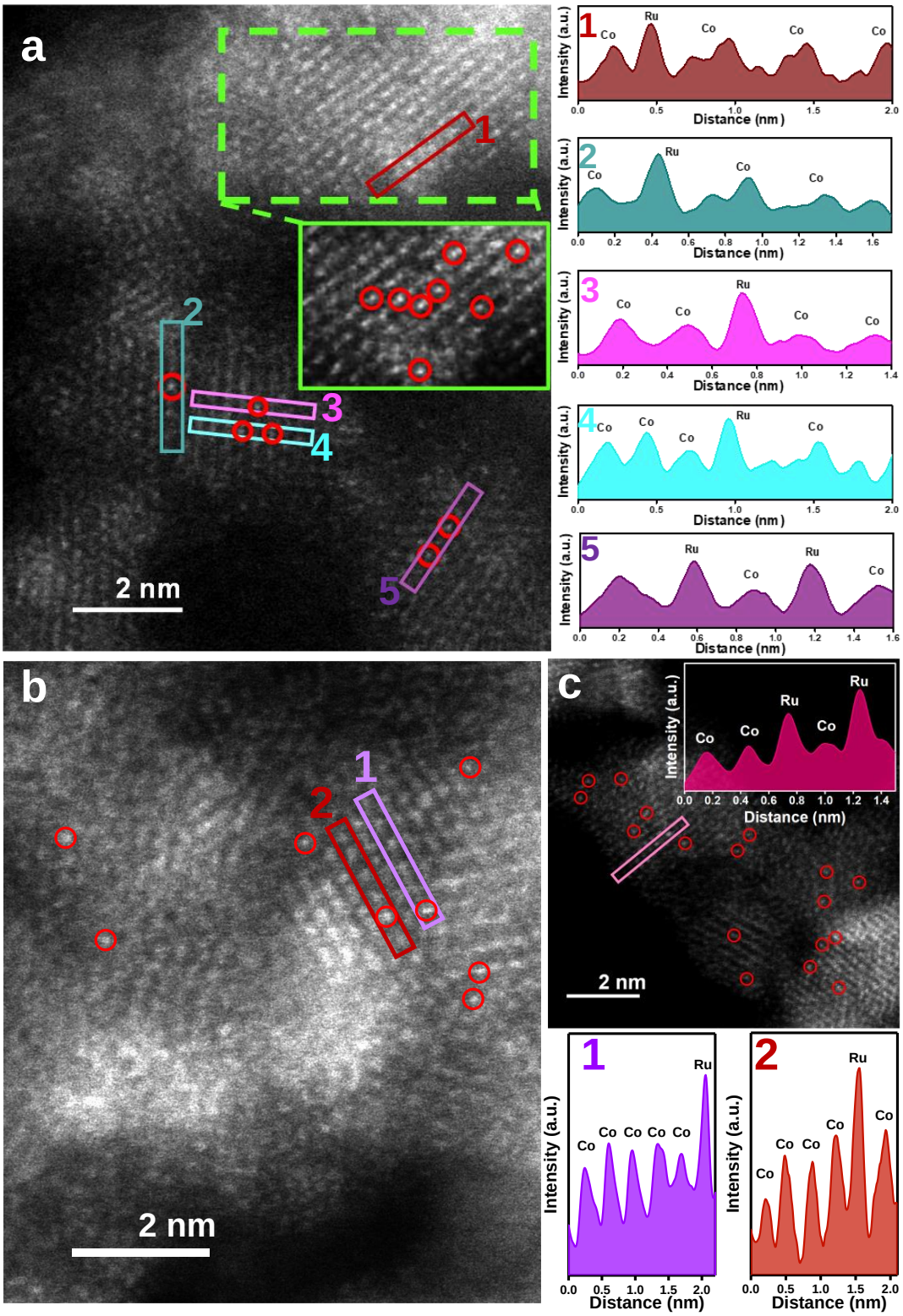

Figure S7. (a-c) HAADF-STEM images of Ru_{SA}-Co_3O_4, the insets show the corresponding intensity distributions marked by dashed boxes of different colors.

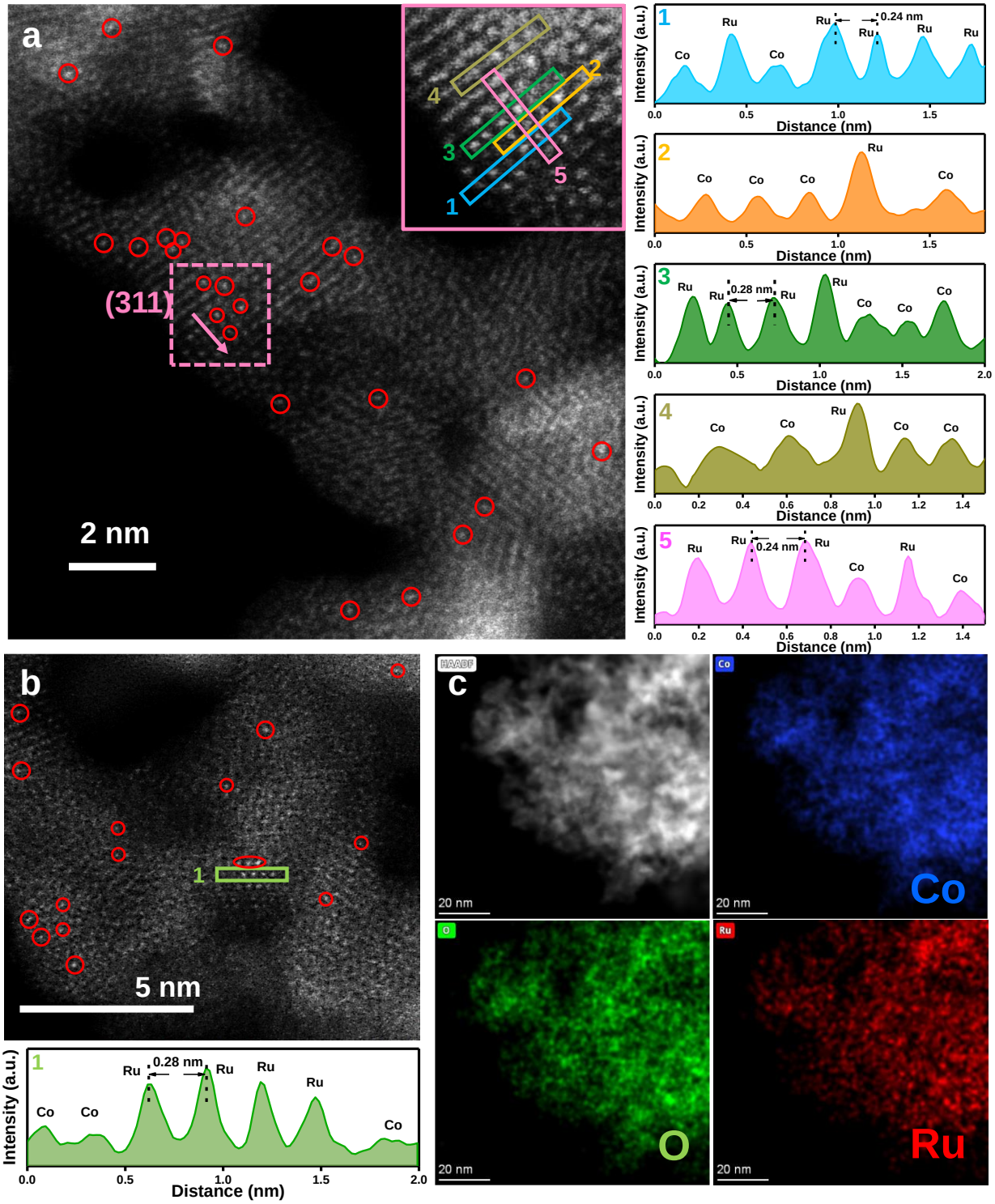

Figure S8. (a, b) HAADF-STEM images of Ru_{SA}-Co_3O_4, the insets show the corresponding intensity distributions marked by dashed boxes of different colors, (c) the element mapping of Ru_{SA}-Co_3O_4.

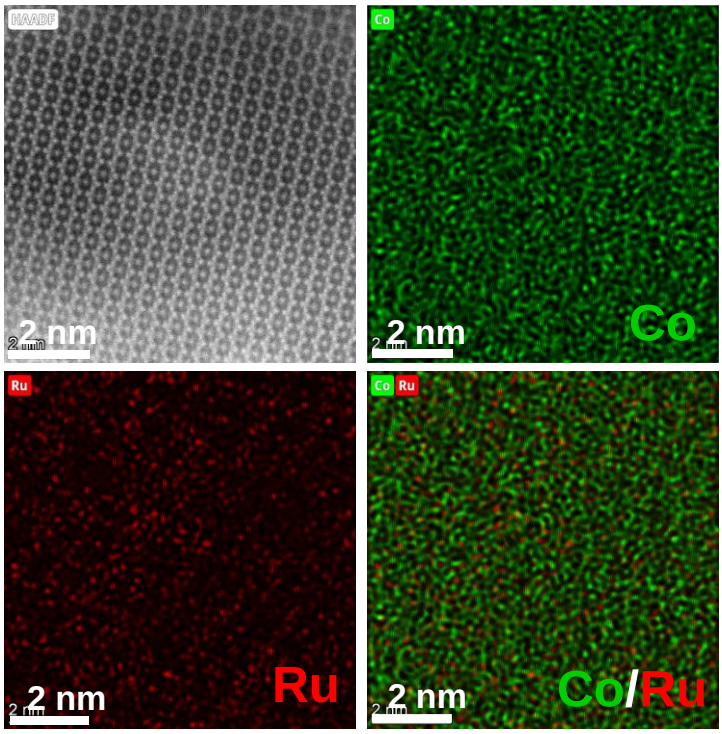

Figure S9. EELS mapping of Ru_{SA}-Co_3O_4.

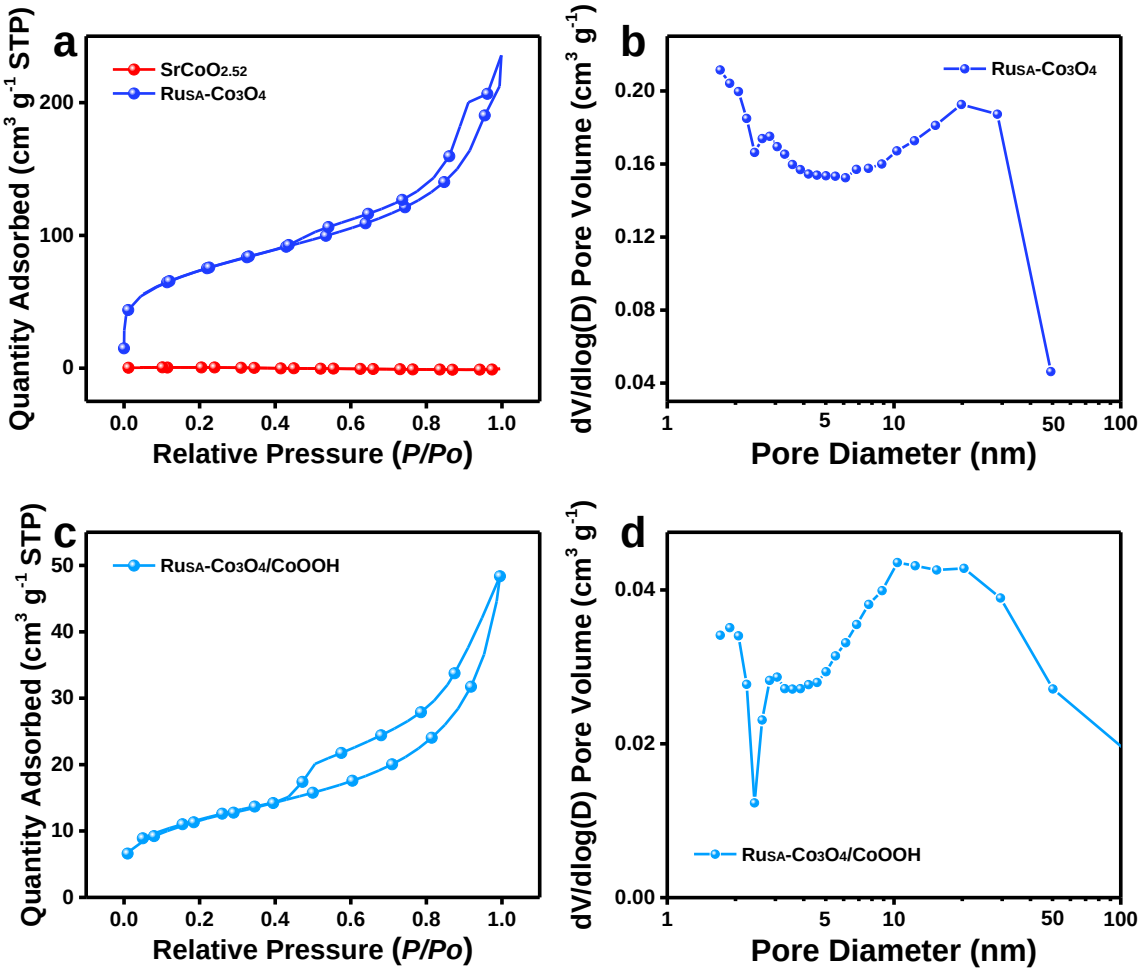

Figure S10. N_2 adsorption-desorption isotherms of (a) $SrCoO_{2.52}$ and Ru_{SA}-Co_3O_4, (c) Ru_{SA}-Co_3O_4/CoOOH. Pore distributions from the adsorption branch: (b) Ru_{SA}-Co_3O_4 and (d) Ru_{SA}-Co_3O_4/CoOOH.

The specific surface area and porosity of catalysts $SrCoO_{2.52}$, Ru_{SA}-Co_3O_4, and Ru_{SA}-Co_3O_4/CoOOH were evaluated by N_2 adsorption and desorption curves. It can be observed that at lower relative pressures ($P/P_0 < 0.015$), the isotherm of Ru_{SA}-Co_3O_4 showed a sharp rise, indicating that the micropores in the catalyst were sequentially filled (Figure S10a). As the relative pressure increases ($P/P_0 > 0.4$), the catalyst showed obvious hysteresis curve, which is a typical type IV isotherm, reflecting the coexistence of micropores and mesoporous. According to the calculated results, the Barrett-Emmett-Teller (BET) specific surface area and average pore size of Ru_{SA}-Co_3O_4 are 253.56 $m^2 \cdot g^{-1}$ and 6.2 nm, respectively, which are far higher than the 1.47

$m^2 \cdot g^{-1}$ of $SrCoO_{2.52}$ (Figure S10b). Furthermore, $SrCoO_{2.52}$ has almost no pore structure. This indicates that the specific surface area and pore size of the catalyst are greatly improved after the first reconfiguration of perovskite oxides to form Ru single atom-anchored spinel Co_3O_4, which promotes the improvement of catalytic performance. Interestingly, after the second reconstruction of Ru_{SA}-Co_3O_4, the N_2 absorption and desorption curves of Ru_{SA}-Co_3O_4/CoOOH showed type IV isotherms and type H3 hysteresis loops, indicating a large number of mesoporous structures in the catalyst (Figure S10c). Its specific surface area decreased to 40.85 $m^2 \cdot g^{-1}$, while its average pore size increased to 8.4 nm (Figure S10d). The decrease of the specific surface area of Ru_{SA}-Co_3O_4/CoOOH may be due to the pore collapse caused by the reconstruction of a layer of CoOOH on the surface of Ru_{SA}-Co_3O_4, which partially blocked the pore. The large pore size formed by the second reconstruction plays a major role in the OER catalytic reaction, which is conducive to exposing more active sites in contact with the electrolyte, accelerating the diffusion of reactants and products in the channel, and thus promoting the electrochemical process.

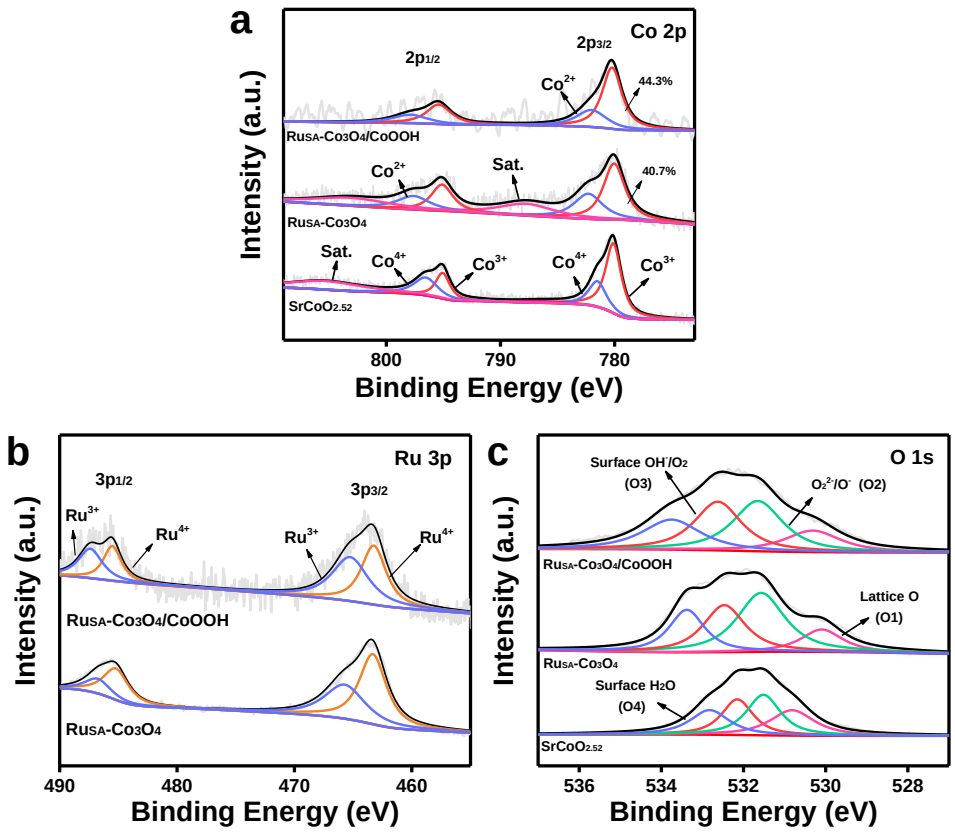

Figure S11. XPS spectra of different catalysts: (a) Co 2p, (b) Ru 3p, and (c) O 1s.

From the XPS spectrum of Co 2p of $SrCoO_{2.52}$, two peaks located at 780.1 eV and 795.1 eV are attributed to $2p_{3/2}$ and $2p_{1/2}$ of Co^{3+} species, respectively (Figure S11a). Two other peaks with binding energies of 781.6 eV and 796.6 eV are ascribed to $2p_{3/2}$ and $2p_{1/2}$ of Co^{4+} species, respectively. Lattice oxygen (530.8 eV, O1), surface-adsorbed superoxide oxygen (O_2^{2-}/O^-, 531.6 eV, O2), hydroxyl or surface-adsorbed oxygen (-OH/O_2, 532.2 eV, O3), and the H_2O molecules physically adsorbed or chemically adsorbed (532.8 eV, O4) can be found from the XPS spectrum of O 1s in $SrCoO_{2.52}$ (Figure S11c). Among them, the high reactive oxygen species O_2^{2-}/O^- at 531.6 eV was associated with oxygen defects on the catalyst surface.

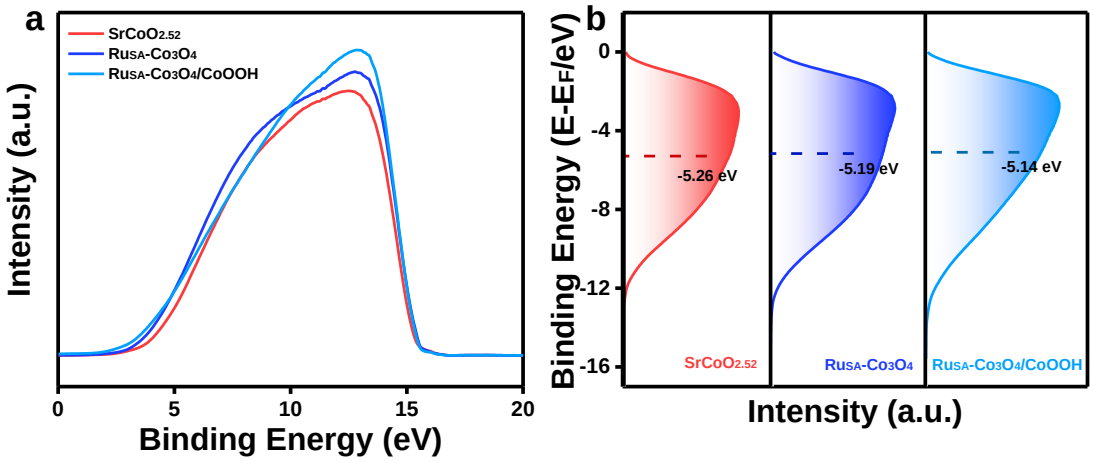

Figure S12. (a) UPS spectra of different catalysts, (b) the surface valence band photoemission spectra of different catalysts.

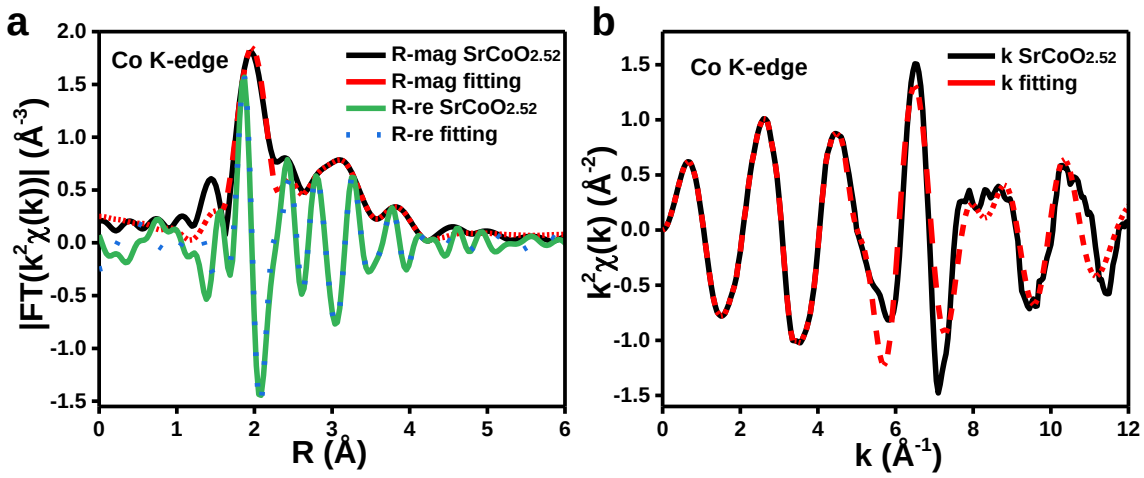

Figure S13. (a) Fitting curves of Co K-edge EXAFS of $SrCoO_{2.52}$ in *R*-space. (b) Fitting curves of Co K-edge EXAFS of $SrCoO_{2.52}$ in the *K*-space.

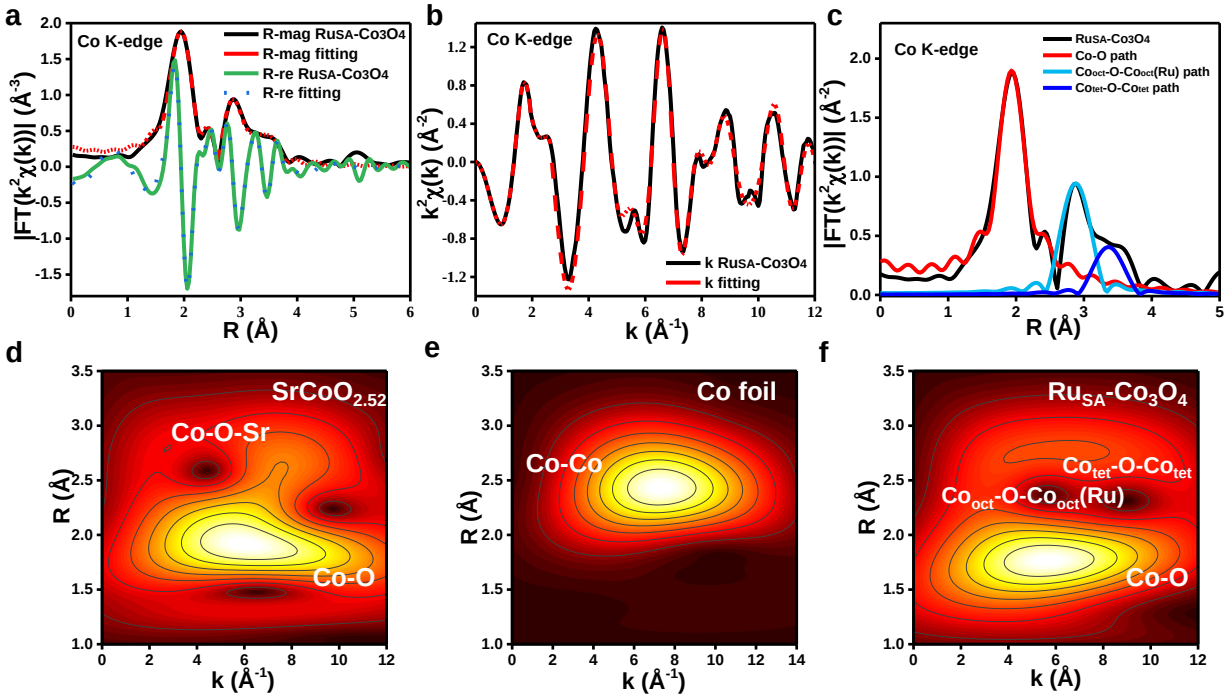

Figure S14. (a) Fitting curves of Co K-edge EXAFS of Ru_{SA}-Co_3O_4 in the *R*-space. (b) Fitting curves of Co K-edge EXAFS of Ru_{SA}-Co_3O_4 in the *K*-space. (c) Scattering path of Ru_{SA}-Co_3O_4 Co K-edge. Wavelet transforms for the k^3-weighted Co K-edge EXAFS signals of (d) $SrCoO_{2.52}$ (e) Co-foil, and (f) Ru_{SA}-Co_3O_4, respectively.

The k^2-weighted Co K-edge EXAFS is analyzed by best fit, and the structural parameters can be extracted (Figures S13 and S14). As seen from phase-corrected Fourier transform-extended X-ray absorption fine structure (FT-EXAFS) spectra of $SrCoO_{2.52}$, three prominent peaks located at 1.8 Å and 3.0 Å can be attributed to the Co-O coordination in the first shell, Co-O-Sr coordination in the second shell, respectively (Figure 2c, Figure S13a, b, and Table S3). Meanwhile, Figure S14c demonstrates three scattering paths for the Co-O, Co_{oct}-O-Co_{oct}(Ru), and Co_{tet}-O-Co_{tet} bands, indicating a successful phase structure transition from perovskite to spinel.

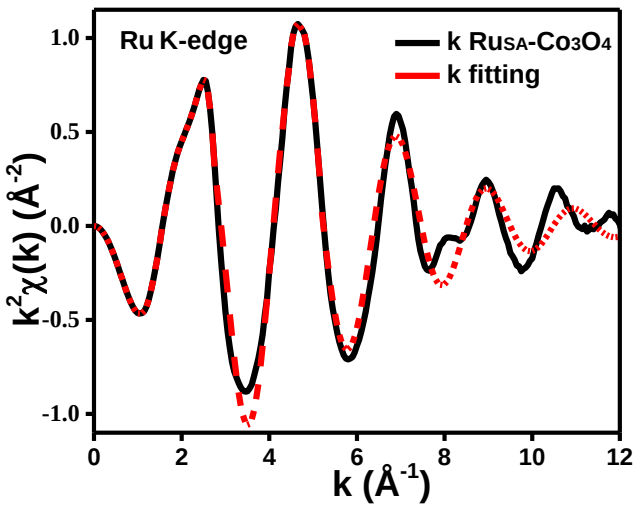

Figure S15. Fitting curves of Ru K-edge EXAFS of Ru_{SA}-Co_3O_4 in the *K*-space.

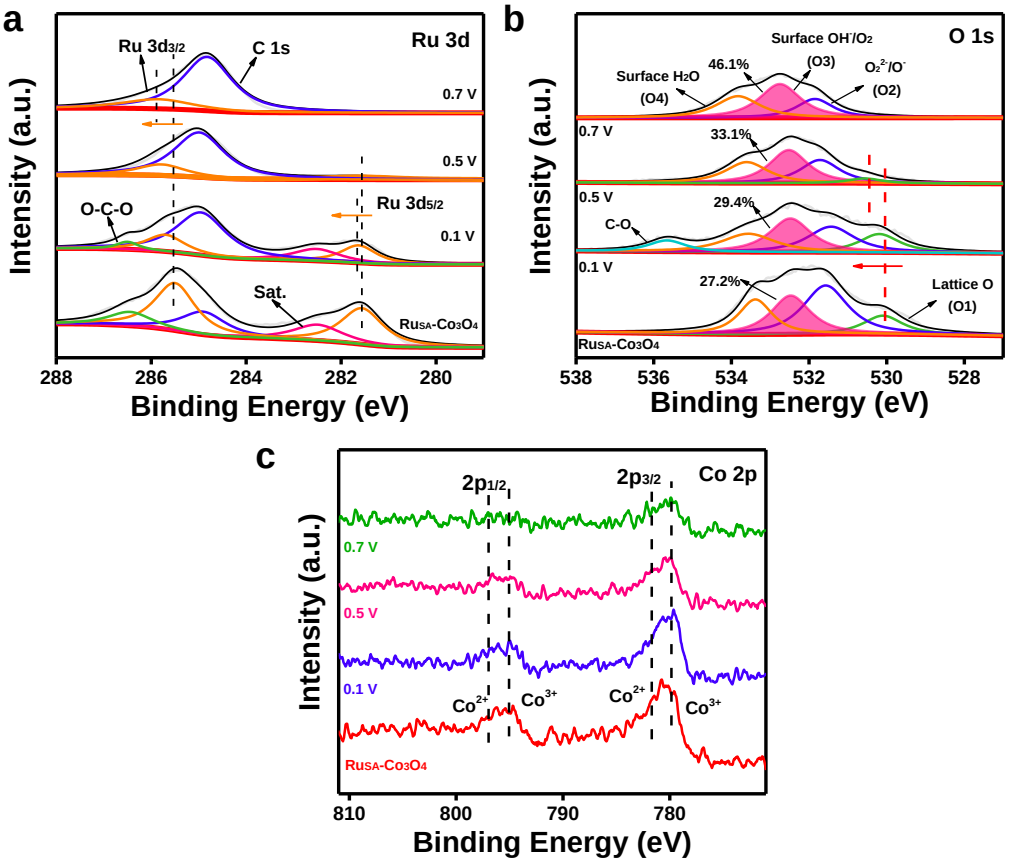

Figure S16. XPS spectra of different voltages: (a) Ru 3d, (b) O 1s, and (c) Co 2p.

In XPS spectra of Ru 3d, the binding energies of 281.5 eV and 285.6 eV are attributed to Ru $3d_{5/2}$ and Ru $3d_{3/2}$ of Ru^{4+}, respectively (Figure S16a).

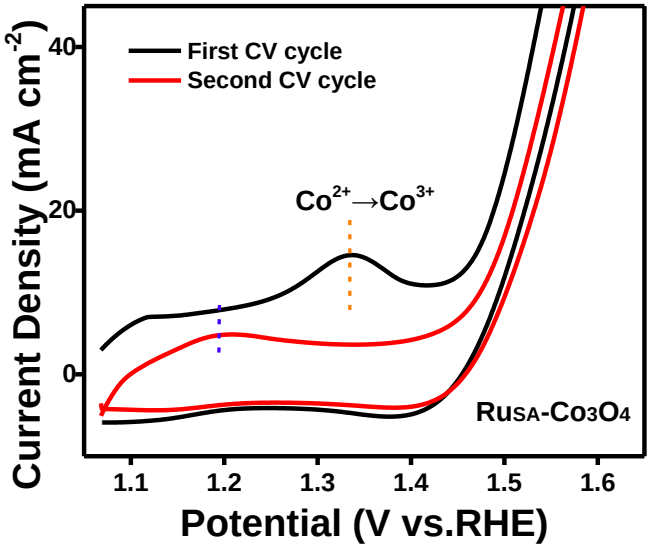

Figure S17. The cyclic voltammetry (CV) curves of Ru_{SA}-Co_3O_4 in 1 M KOH with a scan rate of 10 mV·s^{-1}.

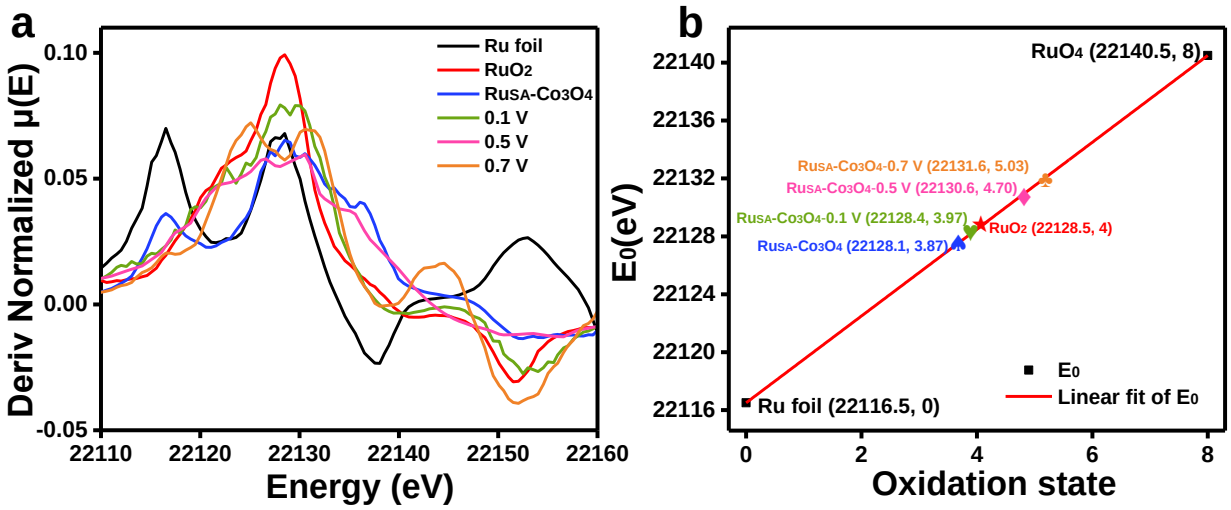

Figure S18. (a) First derivative of Ru K-edge for different catalysts, (b) precise oxidation state determination of different catalysts by linear fitting calibration.

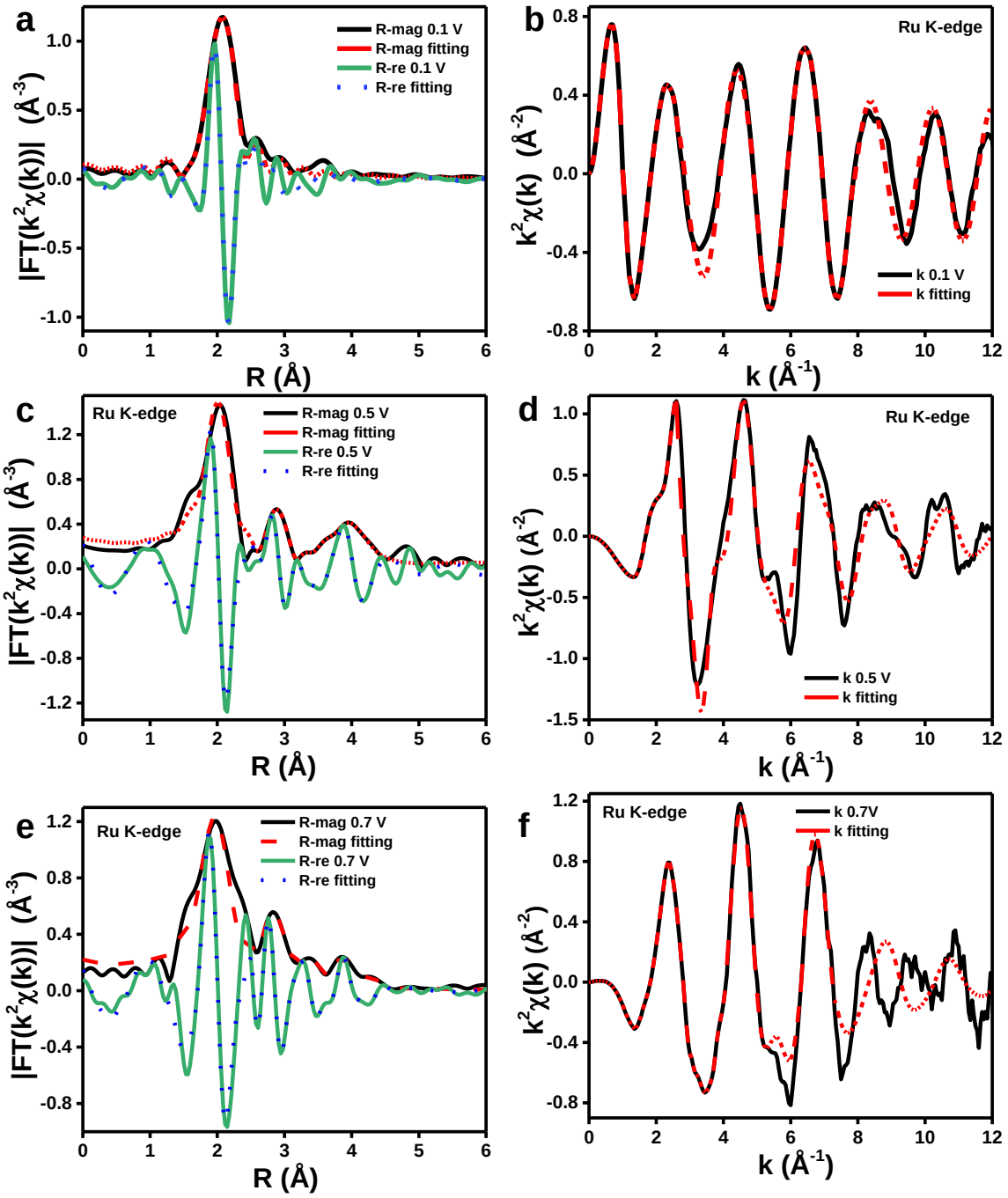

Figure S19. The EXAFS fitting curves of Ru K-edge of Ru_{SA}-Co_3O_4/CoOOH in *R*-space at different voltages: (a) 0.1 V, (c) 0.5 V, and (e) 0.7 V. The EXAFS fitting curves of Ru K-edge of Ru_{SA}-Co_3O_4/CoOOH in *K*-space at different voltages: (b) 0.1 V, (d) 0.5 V, and (f) 0.7 V.

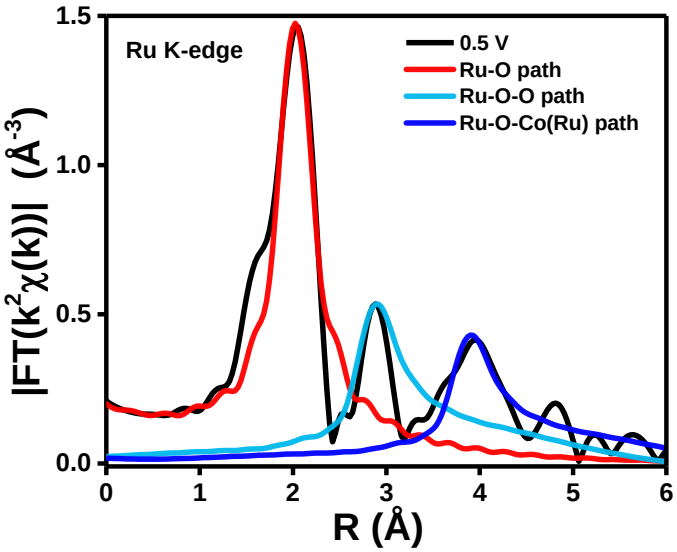

Figure S20. Scattering path of Ru_{SA}-Co_3O_4/CoOOH Ru K-edge at 0.5 V.

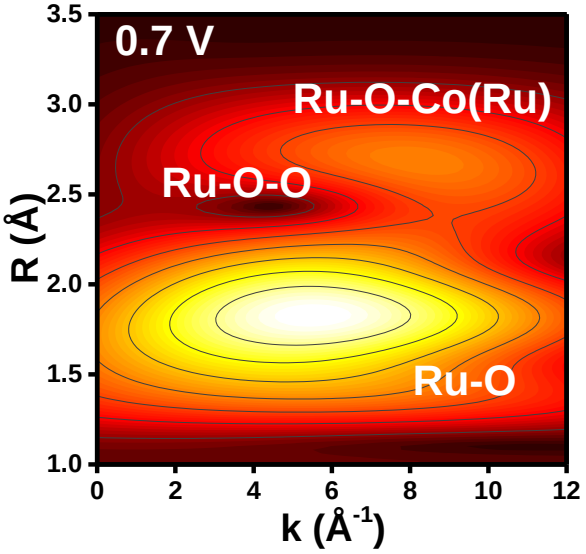

Figure S21. Wavelet transforms for the k^3-weighted Ru K-edge EXAFS signals of Ru_{SA}-Co_3O_4/CoOOH at 0.7 V.

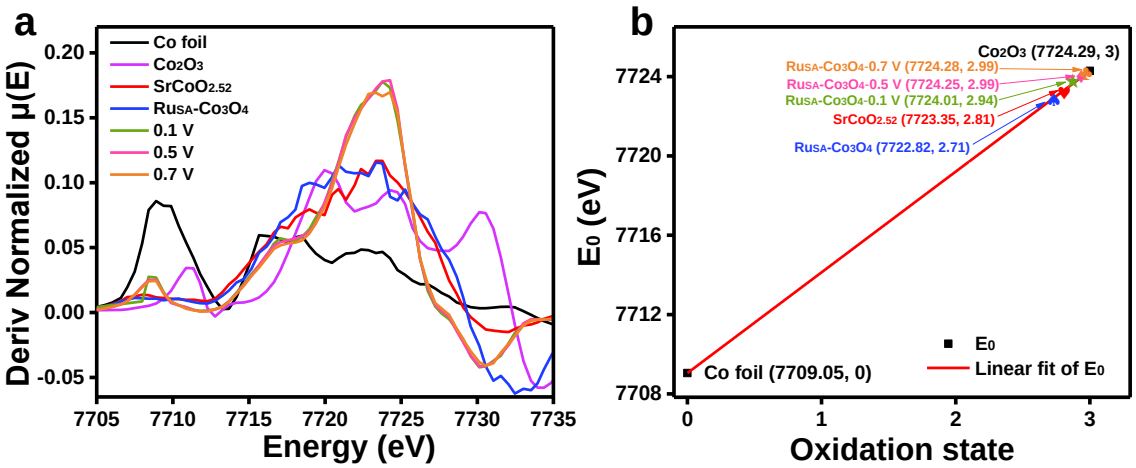

Figure S22. (a) First derivative of Co K-edge for different catalysts, (b) precise oxidation state determination of different catalysts by linear fitting calibration.

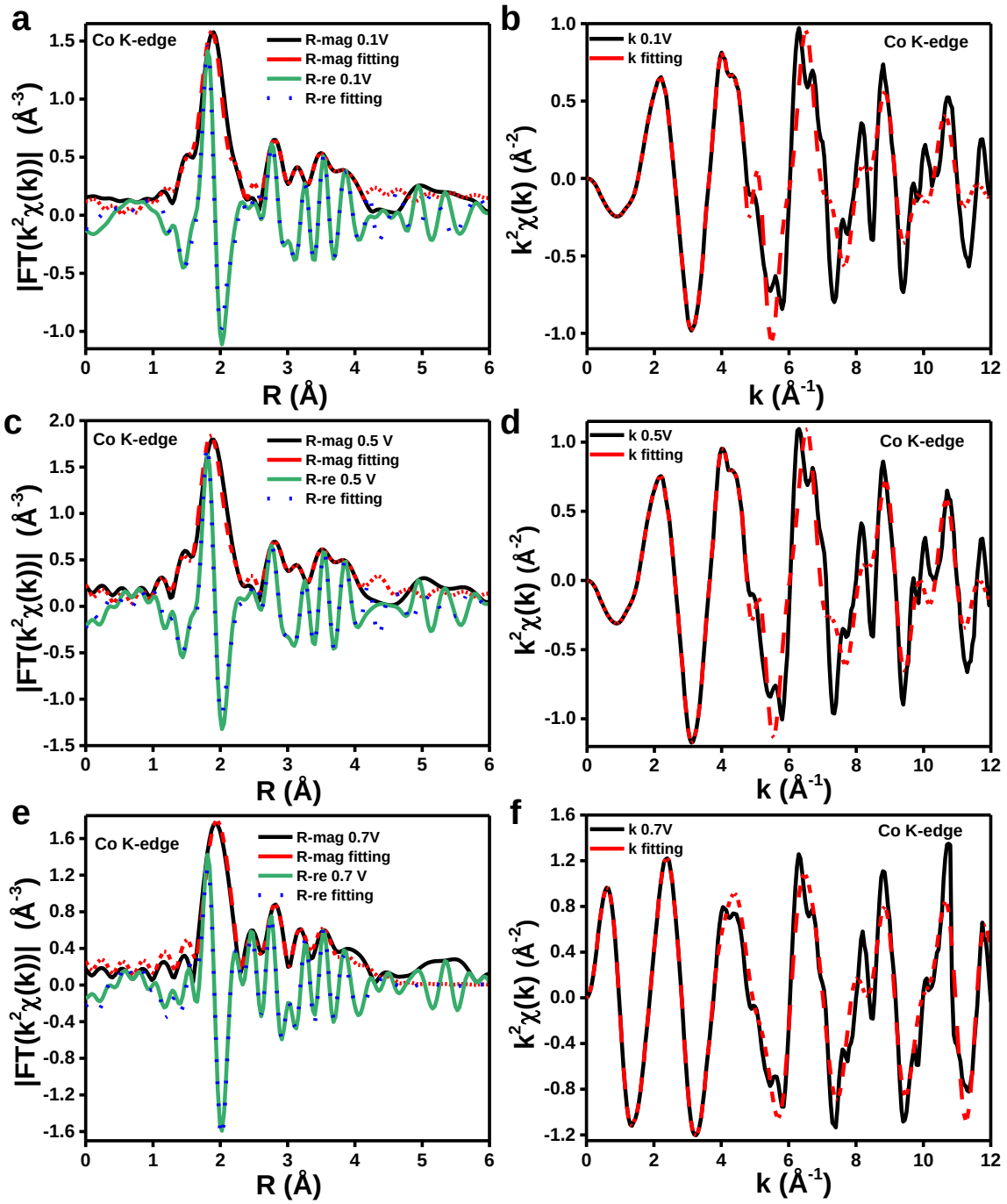

Figure S23. The EXAFS fitting curves of Co K-edge of Ru_{SA}-Co_3O_4/CoOOH in *R*-space at different voltages: (a) 0.1 V, (c) 0.5 V, and (e) 0.7 V. The EXAFS fitting curves of Co K-edge of Ru_{SA}-Co_3O_4/CoOOH in *K*-space at different voltages: (b) 0.1 V, (d) 0.5 V, and (f) 0.7 V.

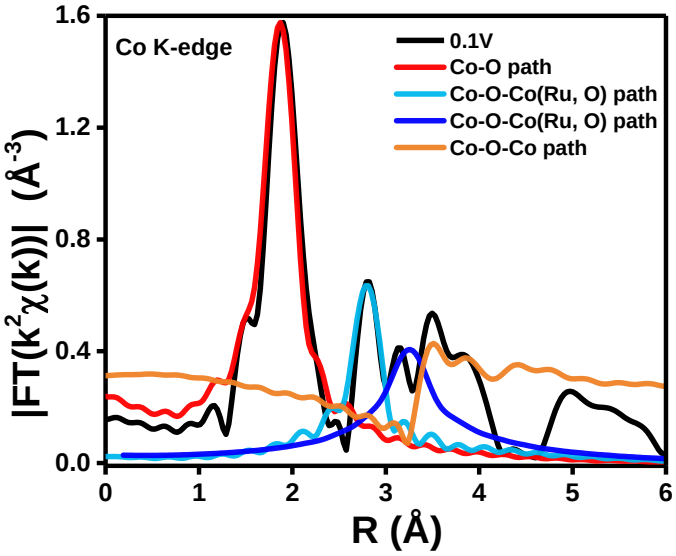

Figure S24. Scattering path of Ru_{SA}-Co_3O_4/CoOOH Co K-edge at 0.1 V.

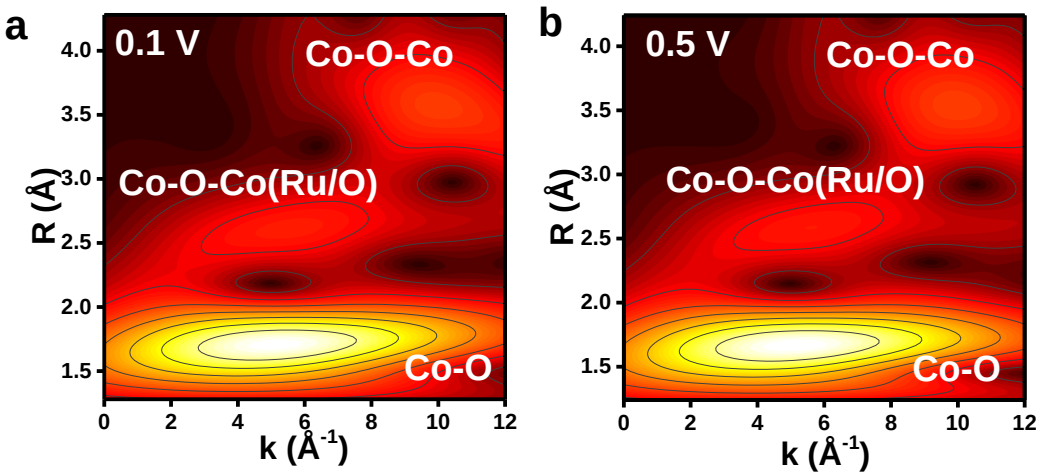

Figure S25. Wavelet transforms for the k^3-weighted Co K-edge EXAFS signals of Ru_{SA}-Co_3O_4/CoOOH at (a) 0.1 V and (b) 0.5 V.

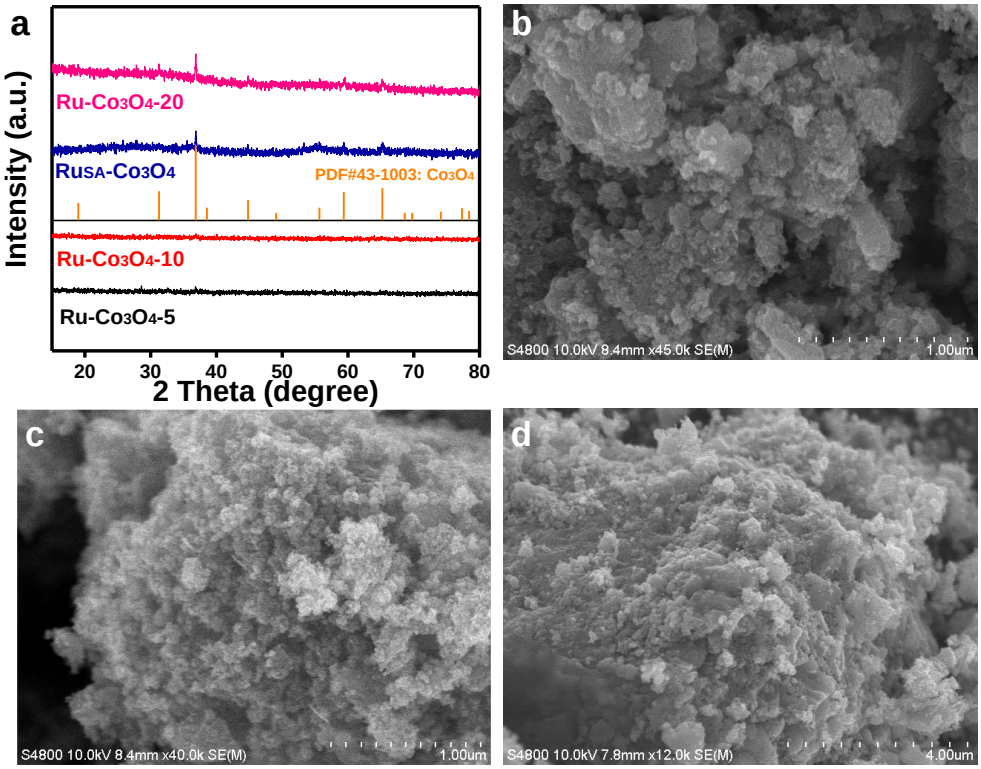

Figure S26. (a) XRD patterns of Ru_{SA}-Co_3O_4 catalyst synthesized with different amounts of Ru^{3+}. SEM images of (b) Ru-Co_3O_4-5, (c) Ru-Co_3O_4-10, and (d) Ru-Co_3O_4-20.

The effect of Ru content (5-20 mL) on structural reconstruction has been also studied. XRD results show that the $SrCoO_{2.52}$ catalyst turns into an amorphous structure when less Ru^{3+} is introduced, which indicates the introduction of Ru^{3+} will eventually lead to the collapse of the $SrCoO_{2.52}$ structure (Figure S26). However, the spinel phase of the Co_3O_4 can be obviously obtained and the diffraction intensity increases with the increase of Ru^{3+} content, further demonstrating that the Ru^{3+} can induce the crystal phase reconstruction of the $SrCoO_{2.52}$ catalyst.

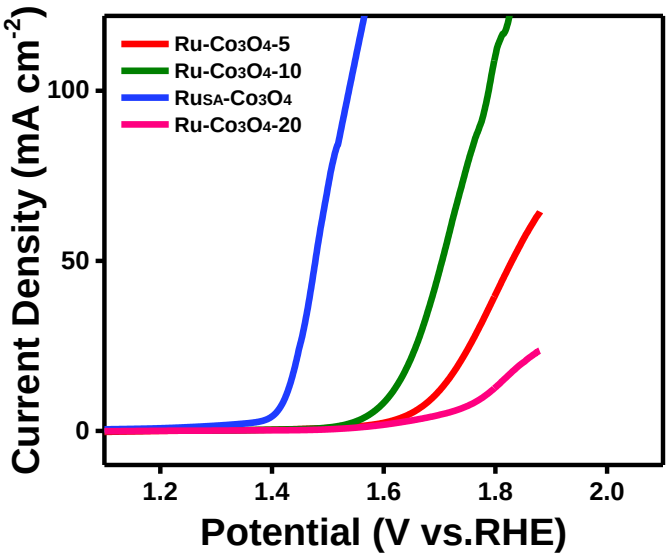

Figure S27. OER performance of catalysts synthesized with different amounts of Ru^{3+}.

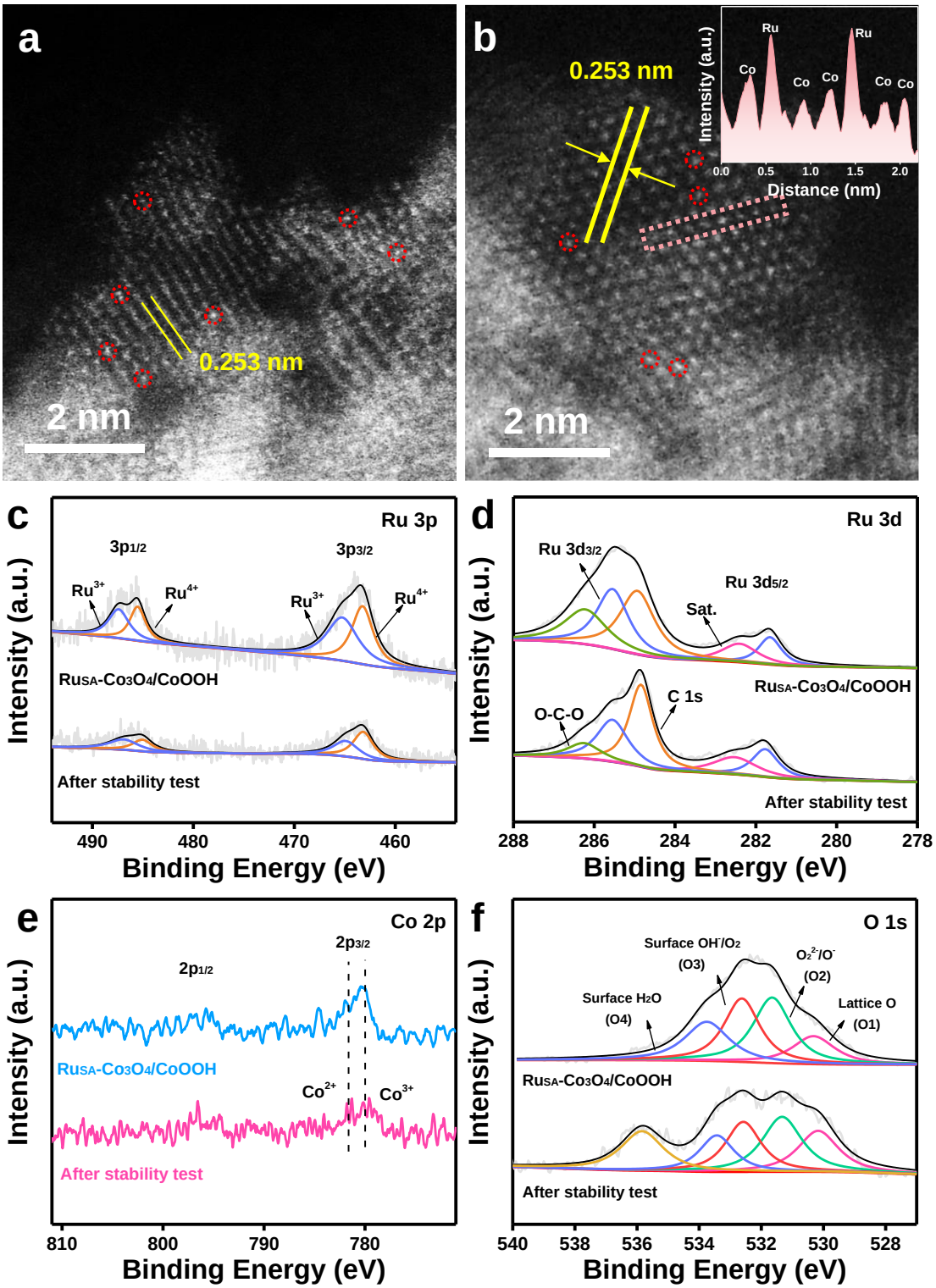

Figure S28. (a, b) HAADF-STEM images of Ru_{SA}-Co_3O_4/CoOOH after stability test. XPS spectra of Ru_{SA}-Co_3O_4/CoOOH after stability test: (c) Ru 3p, (d) Ru 3d, (e) Co 2p, and (f) O 1s.

To verify the structural stability of Ru_{SA}-Co_3O_4/CoOOH in the electrolyte. The catalyst was characterized by XPS and HAADF-STEM after stability test. After a long stability test, STEM images of Ru_{SA}-Co_3O_4/CoOOH show a crystal face spacing of 0.253 nm, which is little changed compared to the catalyst before stability. And a large number of white bright spots indicate that Ru single atoms are still stably anchored in the substrate lattice array (Figure S28a, b). Furthermore, the surface electronic structure of the Ru_{SA}-Co_3O_4/CoOOH catalyst before and after stability was studied by XPS spectroscopy. The characteristic peaks of the high-resolution XPS spectra of Ru 3p at 463.2 eV and 465.1eV correspond to Ru^{3+} and Ru^{4+}, respectively (Figure S28c). In the Ru 3d XPS spectrum, the binding energy peaks of 281.5 eV and 285.6 eV are attributed to Ru $3d_{5/2}$ and Ru $3d_{3/2}$ of Ru^{4+}, respectively (Figure S28d). The characteristic peak at 780.3 eV in the Co 2p XPS spectrum of the catalyst corresponds to Co $2p_{3/2}$ of Co_3O_4, further indicating a stable structure of Ru_{SA}-Co_3O_4/CoOOH (Figure S28e). At the same time, lattice oxygen (Metal-O, 530.2 eV, O1), surface-adsorbed superoxide oxygen (O_2^{2-}/O^-, 531.6 eV, O2), hydroxyl or surface-adsorbed oxygen (-OH/O_2, 532.6 eV, O3), and the H_2O molecules physically adsorbed or chemically adsorbed (533.7 eV, O4) can be fitted in the O 1s XPS spectra (Figure S28f). Hence, after a long-term stability test in the alkaline electrolyte, the characteristic peaks of each element in the catalyst did not shift significantly, indicating that Ru_{SA}-Co_3O_4/CoOOH has a stable electronic structure. However, Ru and Co species dissolved to different degrees in the test process due to their own physical and chemical modifications.

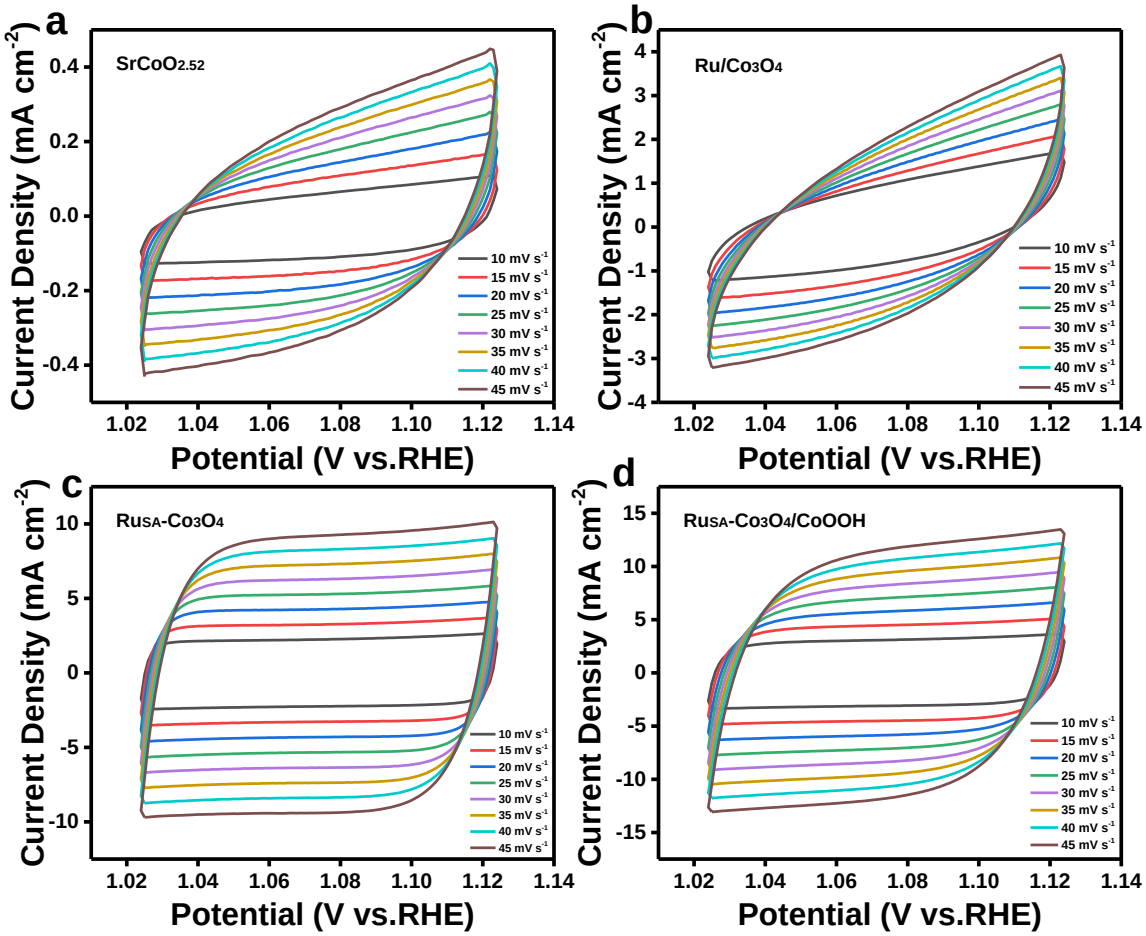

Figure S29. CV cycles at different scanning speeds: (a) $SrCoO_{2.52}$, (b) Ru/Co_3O_4, (c) Ru_{SA}-Co_3O_4, and (d) Ru_{SA}-Co_3O_4/CoOOH.

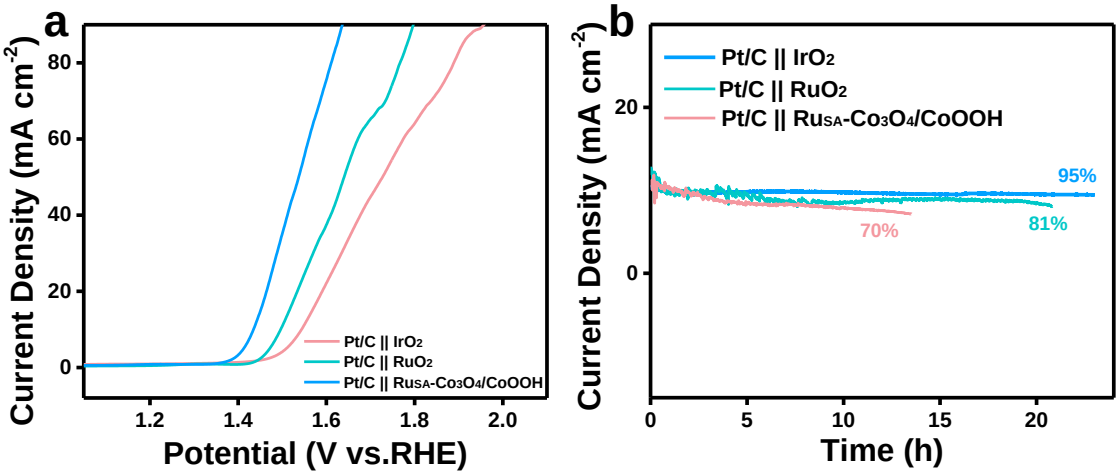

Figure S30. (a) Water splitting LSV curve of Pt/C||Ru_{SA}-Co_3O_4/CoOOH, Pt/C||RuO_2, and Pt/C||IrO_2. (b) Chronoamperometry durability test.

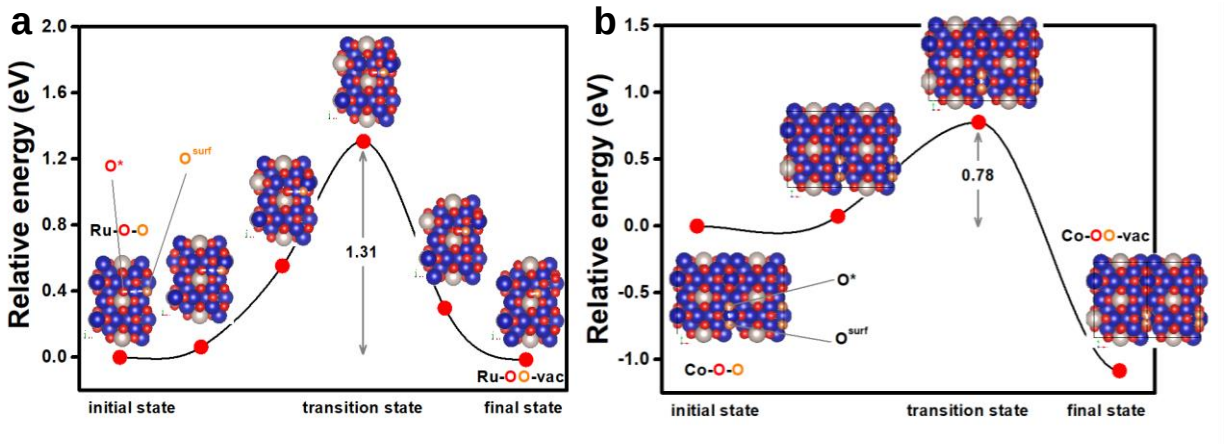

Figure S31. On the competition between AEM and LOM for OER. The energy barrier for O*-O^{surf} bond formation on (a) Ru and (b) Co sites of the Ru_{SA}-Co_3O_4 catalyst.

The optimized atomic geometries of the initial, transition and final states are shown in the insets. The gray, blue, and red (orange) spheres represent Ru, Co, and O atoms, respectively. Recently, the LOM, in which the surface lattice oxygen (O^{surf}) participates in the OER reaction, has been found favorable for weak binding perovskites.[8-11] In LOM, the nonelectrochemical O*-O^{surf} coupling is a key step for the lattice oxygen to participate the reaction.[9] Herein, we first examine the kinetic feasibility of O*-O^{surf} coupling on Ru_{SA}-Co_3O_4 using Climbing Image Nudged Elastic Band (CI-NEB) method.[12] As shown in Figure S31, although the reaction is exothermic, the activation barrier for the O*-O^{surf} coupling (i.e., the formation of O-O bond) is calculated as 1.31 and 0.78 eV on the Ru and Co sites, respectively, which cannot be surmounted at the room-temperature condition.[13] This demonstrates that although the lattice oxygen can be detached from the Ru_{SA}-Co_3O_4 surface to form oxygen vacancies as evidenced in our EXAFS analysis, it is difficult for lattice oxygen to participate in the O-O coupling directly. On the other hand, although the Ru-OO coordination has been identified in EXAFS, we find that the desorption of OO* from Ru-OO to form Ru + O_2 is highly endothermic (2.22 eV) on the Ru site with oxygen vacancy (Figure S32), suggesting that the Ru-OO coordination would not participate OER but just act as an ancillary in AEM. Note that the O_2 formation (through AEM) and desorption on the oxygen-vacancy Ru site is thermodynamically more feasible (0.42 eV) than the Ru-O-O → Ru + O_2 reaction (Figure S32). These results suggest that the AEM is more favorable than the LOM for OER on the Ru_{SA}-Co_3O_4 catalyst.

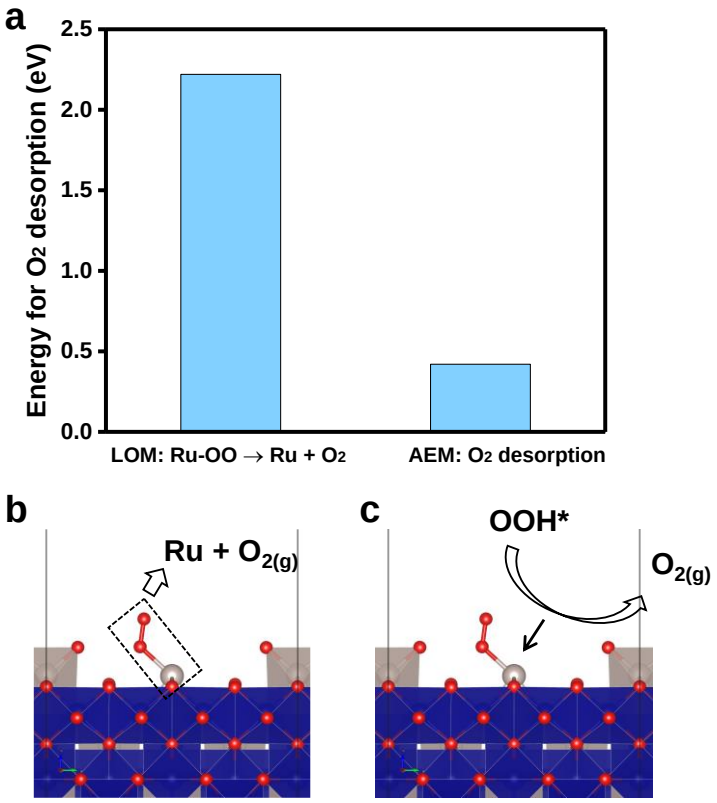

Figure S32. (a) The energy required for O_2 desorption in the Ru-OO → Ru + $O_{2(g)}$ reaction of LOM and the conventional AEM. (b) Model of LOM mechanism. (c) Model of AEM mechanism.

Table S1. ICP-OES result of Ru_{SA}-Co_3O_4.

Catalyst	**Ru (wt %)**
Ru_{SA}-Co_3O_4	7.7

Table S2. Structural parameters extracted from the Co K-edge EXAFS fitting.

	Reduced Chi-square (χ_v^2)	**R-factor（%）**	**amp/ S_0^2**	**$N_{(Co-O\ path)}$**	**$R_{(Co-O\ path)}$ (Å)**	**$\sigma^2_{(Co-O\ path)}$ ($10^{-3}Å^2$)**	**ΔE_0 (eV)**
$SrCoO_{2.52}$	1540.70	0.0502	0.86± 0.13	5	1.965± 0.085	2.9±1.2	2.71±1.28
			amp/ S_0^2	**$N_{(Co-O-Sr\ path)}$**	**$R_{(Co-O-Sr\ path)}$ (Å)**	**$\sigma^2_{(Co-O-Sr\ path)}$ ($10^{-3}Å^2$)**	**ΔE_0 (eV)**
			1.07± 0.15	2	2.998± 0.088	3.3±1.3	3.56±2.19
	Reduced Chi-square (χ_v^2)	**R-factor（%）**	**amp/ S_0^2**	**$N_{(Co-O\ path)}$**	**$R_{(Co-O\ path)}$ (Å)**	**$\sigma^2_{(Co-O\ path)}$ ($10^{-3}Å^2$)**	**ΔE_0 (eV)**
Ru_{SA}-Co_3O_4	989.03	0.0051	0.86± 0.06	6	1.929± 0.011	2.6±0.8	2.73±0.89
			amp/ S_0^2	**$N_{(Co-O-Co\ path)}$**	**$R_{(Co-O-Co\ path)}$ (Å)**	**$\sigma^2_{(Co-O-Co\ path)}$ ($10^{-3}Å^2$)**	**ΔE_0 (eV)**
			0.83± 0.15	2	2.859± 0.017	2.2±1.1	2.68±1.18
			amp/ S_0^2	**$N_{(Co-O-Ru\ path)}$**	**$R_{(Co-O-Ru\ path)}$ (Å)**	**$\sigma^2_{(Co-O-Ru\ path)}$ ($10^{-3}Å^2$)**	**ΔE_0 (eV)**
			0.81± 0.14	1	2.889± 0.014	2.5±1.2	2.22±1.61
			amp/ S_0^2	**$N_{(Co-O-Co\ path)}$**	**$R_{(Co-O-Co\ path)}$ (Å)**	**$\sigma^2_{(Co-O-Co\ path)}$ ($10^{-3}Å^2$)**	**ΔE_0 (eV)**
			0.83± 0.15	1	3.353± 0.021	2.2±1.1	2.68±1.18

[a]*N*: coordination numbers; [b]*R*: bond distance; [c]σ^2: Debye-Waller factors; [d] ΔE_0: the inner potential correction. *R* factor: goodness of fit.

Table S3. Structural parameters extracted from the Ru K-edge EXAFS fitting.

	Reduced Chi-square (χ_v^2)	**R-factor（%）**	**amp/ S_0^2**	**$N_{(Ru-O\ path)}$**	**$R_{(Ru-O\ path)}$ (Å)**	**$\sigma^2_{(Ru-O\ path)}$ (10^{-3}Å^2)**	**ΔE_0 (eV)**
Ru_{SA}-Co_3O_4	1175.45	0.0483	1.05± 0.12	5	1.9623± 0.102	2.8±0.8	2.45±1.57

[a]*N*: coordination numbers; [b]*R*: bond distance; [c]σ^2: Debye-Waller factors; [d]ΔE_0: the inner potential correction. *R* factor: goodness of fit.

Table S4. Structural parameters extracted from the Ru K-edge EXAFS fitting at different voltages.

	Reduced Chi-square (χ_v^2)	**R-factor (%)**	**amp/ S_0^2**	**$N_{(Ru-O\ path)}$**	**$R_{(Ru-O\ path)}$ (Å)**	**$\sigma^2_{(Ru-O\ path)}$ (10^{-3}Å^2)**	**ΔE_0 (eV)**
0.1 V	1032.58	0.0408	1.01± 0.13	5	2.078± 0.062	1.3±0.4	2.83±1.04
	Reduced Chi-square (χ_v^2)	**R-factor (%)**	**amp/ S_0^2**	**$N_{(Ru-O\ path)}$**	**$R_{(Ru-O\ path)}$ (Å)**	**$\sigma^2_{(Ru-O\ path)}$ (10^{-3}Å^2)**	**ΔE_0 (eV)**
0.5 V	1487.11	0.0553	0.87+/- 0.17	6	2.028± 0.121	2.8±1.3	2.84±1.29
			amp/ S_0^2	**$N_{(Ru-O-O\ path)}$**	**$R_{(Ru-O-O\ path)}$ (Å)**	**$\sigma^2_{(Ru-O-O\ path)}$ (10^{-3}Å^2)**	**ΔE_0 (eV)**
			0.85±- 0.13	2	2.676± 0.182	2.7±1.1	3.82±1.67
			amp/ S_0^2	**$N_{(Ru-O-Ru\ path)}$**	**$R_{(Ru-O-Ru(Co)\ path)}$ (Å)**	**$\sigma^2_{(Ru-O-Ru\ path)}$ (10^{-3}Å^2)**	**ΔE_0 (eV)**
			0.81±0.13	1	3.776± 0.133	3.8±1.4	3.62±1.88
	Reduced Chi-square (χ_v^2)	**R-factor (%)**	**amp/ S_0^2**	**$N_{(Ru-O\ path)}$**	**$R_{(Ru-O\ path)}$ (Å)**	**$\sigma^2_{(Ru-O\ path)}$ (10^{-3}Å^2)**	**ΔE_0 (eV)**
0.7 V	1886.22	0.0568	1.02± 0.14	5	1.996± 0.111	2.5±1.5	2.07±0.48
			amp/ S_0^2	**$N_{(Ru-O-O\ path)}$**	**$R_{(Ru-O-O\ path)}$ (Å)**	**$\sigma^2_{(Ru-O-O\ path)}$ (10^{-3}Å^2)**	**ΔE_0 (eV)**
			0.85± 0.13	3	2.676± 0.145	2.7±1.3	2.46±1.17
			amp/ S_0^2	**$N_{(Ru-O-Ru\ path)}$**	**$R_{(Ru-O-Ru(Co)\ path)}$ (Å)**	**$\sigma^2_{(Ru-O-Ru\ path)}$ (10^{-3}Å^2)**	**ΔE_0 (eV)**
			0.80± 0.12	0.8	3.714± 0.158	3.8±1.2	3.39±1.77

Table S5. Structural parameters extracted from the Co K-edge EXAFS fitting at 0.1 V.

	Reduced Chi-square (χ_v^2)	**R-factor (%)**	**amp/ S_0^2**	**$N_{(Co-O\ path)}$**	**$R_{(Co-O\ path)}$ (Å)**	**$\sigma^2_{(Co-O\ path)}$ (10^{-3}Å^2)**	**ΔE_0 (eV)**
Ru_{SA}-Co_3O_4/CoOOH	1478.73	0.0541	0.86± 0.06	4	1.898± 0.112	2.6+/-1.4	2.38+/ -1.45
			amp/ S_0^2	**$N_{(Co-O-O\ path)}$**	**$R_{(Co-O-O\ path)}$ (Å)**	**$\sigma^2_{(Co-O-O\ path)}$ (10^{-3}Å^2)**	**ΔE_0 (eV)**
			0.81± 0.13	1	2.685± 0.124	2.7±1.1	2.74± 1.13
			amp/ S_0^2	**$N_{(Co-O-Co\ path)}$**	**$R_{(Co-O-Co\ path)}$ (Å)**	**$\sigma^2_{(Co-O-Co\ path)}$ (10^{-3}Å^2)**	**ΔE_0 (eV)**
			0.83±0.1 5	1	2.823± 0.122	2.3±1.2	3.54± 1.25
			amp/ S_0^2	**$N_{(Co-O-Ru\ path)}$**	**$R_{(Co-O-Ru\ path)}$ (Å)**	**$\sigma^2_{(Co-O-Ru\ path)}$ (10^{-3}Å^2)**	**ΔE_0 (eV)**
			0.81±0.1 4	0.5	2.878± 0.081	3.3±1.4	3.23± 1.54
			amp/ S_0^2	**$N_{(Co-O-Co\ path)}$**	**$R_{(Co-O-Co\ path)}$ (Å)**	**$\sigma^2_{(Co-O-Co\ path)}$ (10^{-3}Å^2)**	**ΔE_0 (eV)**
			0.83±0.1 5	1	3.379± 0.101	2.3±1.2	3.54± 1.25
			amp/ S_0^2	**$N_{(Co-O-Co\ path)}$**	**$R_{(Co-O-Co\ path)}$ (Å)**	**$\sigma^2_{(Co-O-Co\ path)}$ (10^{-3}Å^2)**	**ΔE_0 (eV)**
			0.83± 0.15	1	3.671± 0.103	2.3±1.2	3.54± 1.25

Table S6. Structural parameters extracted from the Co K-edge EXAFS fitting at 0.5 V.

	Reduced Chi-square (χ_v^2)	R-factor (%)	amp/ S_0^2	$N_{(Co\text{-}OH\ path)}$	$R_{(Co\text{-}OH\ path)}$ (Å)	$\sigma^2_{(Co\text{-}OH\ path)}$ (10^{-3}Å^2)	ΔE_0 (eV)
Ru_{SA}-Co_3O_4/CoOOH	1578.68	0.0513	0.92+/-0.11	6	1.921± 0.113	2.5+/-1.3	-2.22+/-1.05
			amp/ S_0^2	**$N_{(Co\text{-}O\text{-}O\ path)}$**	**$R_{(Co\text{-}O\text{-}O\ path)}$ (Å)**	**$\sigma^2_{(Co\text{-}O\text{-}O\ path)}$ (10^{-3}Å^2)**	**ΔE_0 (eV)**
			0.81+/-0.13	1	2.685± 0.117	2.5+/-1.2	2.85+/-1.18
			amp/ S_0^2	**$N_{(Co\text{-}O\text{-}Co\ path)}$**	**$R_{(Co\text{-}O\text{-}Co\ path)}$ (Å)**	**$\sigma^2_{(Co\text{-}O\text{-}Co\ path)}$ (10^{-3}Å^2)**	**ΔE_0 (eV)**
			0.83+/-0.15	1	2.823± 0.108	2.3+/-1.2	3.56+/-1.21
			amp/ S_0^2	**$N_{(Co\text{-}O\text{-}Ru\ path)}$**	**$R_{(Co\text{-}O\text{-}Ru\ path)}$ (Å)**	**$\sigma^2_{(Co\text{-}O\text{-}Ru\ path)}$ (10^{-3}Å^2)**	**ΔE_0 (eV)**
			0.81+/-0.14	0.5	2.877± 0.084	3.6+/-0.8	3.17+/-1.84
			amp/ S_0^2	**$N_{(Co\text{-}O\text{-}Co\ path)}$**	**$R_{(Co\text{-}O\text{-}Co\ path)}$ (Å)**	**$\sigma^2_{(Co\text{-}O\text{-}Co\ path)}$ (10^{-3}Å^2)**	**ΔE_0 (eV)**
			0.83+/-0.15	1	3.379± 0.106	2.3+/-1.2	3.56+/-1.21
			amp/ S_0^2	**$N_{(Co\text{-}O\text{-}Co\ path)}$**	**$R_{(Co\text{-}O\text{-}Co\ path)}$ (Å)**	**$\sigma^2_{(Co\text{-}O\text{-}Co\ path)}$ (10^{-3}Å^2)**	**ΔE_0 (eV)**
			0.83+/-0.15	1	3.671± 0.105	2.3+/-1.2	3.56+/-1.21

Table S7. Structural parameters extracted from the Co K-edge EXAFS fitting at 0.7 V.

	Reduced Chi-square (χ_v^2)	R-factor (%)	amp/ S_0^2	$N_{(Co\text{-}OH\ path)}$	$R_{(Co\text{-}OH\ path)}$ (Å)	$\sigma^2_{(Co\text{-}OH\ path)}$ (10^{-3}Å^2)	ΔE_0 (eV)
Ru_{SA}-Co_3O_4/CoOOH	1578.68	0.0513	0.88+/-0.12	6	1.928± 0.056	2.4+/-1.1	2.35+/-1.43
			amp/ S_0^2	**$N_{(Co\text{-}O\text{-}O\ path)}$**	**$R_{(Co\text{-}O\text{-}O\ path)}$ (Å)**	**$\sigma^2_{(Co\text{-}O\text{-}O\ path)}$ (10^{-3}Å^2)**	**ΔE_0 (eV)**
			0.81+/-0.13	2	2.685± 0.059	2.6+/-1.4	2.25+/-1.37
			amp/ S_0^2	**$N_{(Co\text{-}O\text{-}Co\ path)}$**	**$R_{(Co\text{-}O\text{-}Co\ path)}$ (Å)**	**$\sigma^2_{(Co\text{-}O\text{-}Co\ path)}$ (10^{-3}Å^2)**	**ΔE_0 (eV)**
			0.83+/-0.15	1.5	2.889± 0.071	2.3+/-1.2	3.52+/-1.88
			amp/ S_0^2	**$N_{(Co\text{-}O\text{-}Ru\ path)}$**	**$R_{(Co\text{-}O\text{-}Ru\ path)}$ (Å)**	**$\sigma^2_{(Co\text{-}O\text{-}Ru\ path)}$ (10^{-3}Å^2)**	**ΔE_0 (eV)**
			0.81+/-0.14	0.5	2.877± 0.084	3.1+/-1.3	3.23+/-1.69
			amp/ S_0^2	**$N_{(Co\text{-}O\text{-}Co\ path)}$**	**$R_{(Co\text{-}O\text{-}Co\ path)}$ (Å)**	**$\sigma^2_{(Co\text{-}O\text{-}Co\ path)}$ (10^{-3}Å^2)**	**ΔE_0 (eV)**
			0.83+/-0.15	1	3.379± 0.039	2.3+/-1.2	3.52+/-1.88
			amp/ S_0^2	**$N_{(Co\text{-}O\text{-}Co\ path)}$**	**$R_{(Co\text{-}O\text{-}Co\ path)}$ (Å)**	**$\sigma^2_{(Co\text{-}O\text{-}Co\ path)}$ (10^{-3}Å^2)**	**ΔE_0 (eV)**
			0.83+/-0.15	1	3.671± 0.039	2.3+/-1.2	3.52+/-1.88

Table S8. Comparison of properties of Ru_{SA}-Co_3O_4/CoOOH and noble metal based electrocatalysts in 1 M KOH.

Catalyst	Current density ($mA \cdot cm^{-2}$)	Overpotential (mV)	Reference
Ru_{SA}-Co_3O_4/CoOOH	**10**	**175**	**This work**
$SrCo_{0.5}Ir_{0.5}O_3$	0.4	270	*Sci. Adv.*, 2021, **7,** eabk1788
Ir_1-Co_3O_4-NS-350	10	226	*ACS Catal.*, 2023, **13**, 3757-3767
RhSAC−CuO NAs/CF	10	197	*Nano Lett.*, 2020, **20**, 5482-5489
Ru Co/ELCO	10	247	*Angew. Chem. Int. Ed.*, 2022, e202205946
Ir_1/$CoOOH_{sur}$	10	210	*J. Am. Chem. Soc.*, 2022, **144**, 9271-9279
$Ir_{0.1}$/Ni_9Fe SAC	10	183	*PNAS*, 2021, **118**, e2101817118
Ru-CoOOH/NF	100	330	*ACS Nano*, 2023, **17**, 12422-12432
$(La_{0.8}Sr_{0.2})_{0.9}Co_{0.1}Fe_{0.8}Ru_{0.1}O_{3-\delta}$-3	10	347	*Nano Res.*, 2022, **15**, 6977-6986
RuCu NSs/C-350 ^oC	10	234	*Angew. Chem. Int. Ed.*, 2019, **58**, 13983-13988
Ir-NiO	10	215	*J. Am. Chem. Soc.*, 2020, **142**, 7425-7433
Ir_1/V_O–CoOOH	10	200	*Nat. Commun.*, 2022, **13**, 2473
$Ru_{0.85}Zn_{0.15}O_{2-\delta}$	10	195	*Adv. Energy Mater.*, 2023, **13**, 2300177
$SrTi(Ir)O_3$	10	265	*Angew. Chem. Int. Ed.*, 2020, **59**, 19654

Table S9. Comparison of the OER performance of Ru_{SA}-Co_3O_4/CoOOH and the recently reported perovskite catalysts at a current density of 10 mA·cm^{-2} in alkaline media.

Catalysts	Overpotential (mV vs. RHE)	Ref.
Ru_{SA}-Co_3O_4/CoOOH	**175**	**(This work)**
$MoReS_2$/LSC	210	*ACS Energy Lett.*, 2023, **8**, 1575-1583
$Sr_{0.9}Co_{0.9}Ir_{0.1}O_{3-\delta}$-350	240	*ACS Catal.*, 2023, **13**, 5007-5019
$Sr(Co_{0.8}Fe_{0.2})_{0.7}B_{0.3}O_{3-\delta}$	240	*Adv. Energy Mater.*, 2019, 1900429
$Sr_3NiFeMoO_{9-\delta}$	248	*ACS Energy Lett.*, 2023, **8**, 565–573
Sr_2MgIrO_6	250	*Nat. Commun.*, 2022, **13**, 7935
$Ba_{0.35}Sr_{0.65}Co_{0.8}Fe_{0.2}O_{3-\delta}$	260	*Nat. Commun.*, 2020, **11**, 3376
$LaNiO_3$-FeOOH-1:1	264	*Applied Catalysis B: Environmental*, 2020, **262**, 118291
SrTi(Ir)O_3	265	*Angew. Chem. Int. Ed.*, 2020, **59**, 19654-19658
$La_{0.9}Ce_{0.1}NiO_3$/CP	270	*Adv. Energy Mater.*, 2021, **11**, 2003755
SCFP-NF	290	*Applied Catalysis B: Environmental*, 2020,**272**, 119046
I-BSCF	290	*Nano Energy*, 2022, **99**,107344
LNFO-250 F	292	*Applied Catalysis B: Environmental*, 2023, **330**, 122661
LFNO-II NRs	302	*Angew. Chem. Int. Ed.*, 2019, **58**, 2316-2320
$LaCo_{0.75}Fe_{0.25}O_3$	310	*Small*, 2022, **18**, 2201131

Fe'-LS'C	310	*Energy Environ. Sci.*, 2022, **15**, 3912-3922
$Sr_2Co_{1.5}Fe_{0.5}O_{6-\delta}$	318	*ACS Catal.*, 2021, **11**, 4327-4337
$Bi_5CoTi_3O_{15}$	320	*Nat. Commun.*, 2019, **10**, 1409
L_5M_2Co	325	*Adv. Funct. Mater.*, 2021, **31**, 2101632
3S-LCN-0.5 HoMSs/CR	330	*Angew. Chem. Int. Ed.*, 2020, **59**, 19691-19695
$Bi_{0.15}Sr_{0.85}Co_{0.8}Fe_{0.2}O_{3-\delta}$	330	*Chemical Engineering Journal*, 2023,**451**, 138646-138657
$Sr_{0.95}Ce_{0.05}Fe_{0.9}Ni_{0.1}O_{3-\delta}$	340	*Adv. Funct. Mater.*, 2022, **32**, 211109
V-LCO/Co_3O_4	354	*Nano Lett.*, 2021, **21**, 8166-8174
SNCF-NRs	359	*Adv. Energy Mater.*, 2017,**7**, 1602122
$La_{0.5}Sr_{1.5}Ni_{1-x}Fe_xO_{4\pm\delta}$	360	*Nat. Commun.*, 2018, **9**, 3150
IrO_2	380	——
$NbBaMn_2O_{5.5}$	395	*ACS Catal.*, 2018, **8**, 364-371
Si–SCO	417	*Nat. Commun.*, 2020, **11**, 2002
$LaNiO_3$/GC	440	*Nano Lett.*, 2020, **20**, 2837
$Sr_2Fe_2O_{6-\delta}$	480	*Angew. Chem. Int. Ed.*, 2019, **58**, 2060-2063

Table S10. Comparison of the OER performance of Ru_{SA}-Co_3O_4/CoOOH and the recently reported spinel catalysts at a current density of 10 mA·cm^{-2} in alkaline media.

Catalysts	Overpotential (mV vs. RHE)	Ref.
Ru_{SA}-Co_3O_4/CoOOH	**175**	**(This work)**
$CoFe_{0.25}Al_{1.75}O_4$	70 (10 μA·cm^{-2})	*Nat. Catal.*, 2019, **2**, 763
$NiCo_2S_4$/Fe-2	200	*Nano Energy*, 2020, **78**, 105230
$NiCo_2O_4$/Cu_xO	213	*J. Mater. Chem. A*, 2021, **9**, 14466-14476
$CoMoO_4$/Co_3O_4/NF	219	*Chemical Engineering Journal*, 2021, **426**, 130063
$Ni_xFe_{3-x}O_4$/Ni	225	*ACS Energy Lett.*, 2018, **3**, 1698-1707
$NiCo_2S_4$-4	243	*Adv. Funct. Mater.*, 2019, **29**, 1807031
F-$CoMoO_4$	256	*Applied Catalysis B: Environmental*, 2022, **303**, 120871
HO_{oct}-NFO NC/IF	260	*Adv. Funct. Mater.*, 2022, **32**, 22010
$NiFe_2O_{4-x}$/NMO-25	262	*Applied Catalysis B: Environmental*, 2021, **286**, 119857
Fe-Co_3O_4	262	*Adv. Mater.*, 2020, **32**, 2002235
CeO_2/Co_3O_4	265	*ACS Catal.*, 2019, **9**, 6484-6490
N-Co_3O_4@NC-2	266	*Adv. Funct. Mater.*, 2019, **29**, 1902875
Co_3O_4/CeO_2 NHs	270	*Adv. Mater.*, 2019, **31**, 1900062
CoO/Co_3O_4	270	*Angew. Chem. Int. Ed.*, 2020, **59**, 6929-6935

MoS_2/rFe-$NiCo_2O_4$	270	*J. Am. Chem. Soc.*, 2020, **142**, 50-54
Co_3O_4-Ag@B	270	*Applied Catalysis B: Environmental*, 2021, **298**, 120529
$NiCo_{2-x}Fe_xO_4$ NBs	274	*Angew. Chem. Int. Ed.*, 2021, **60**, 11841-11846
NiO/$NiFe_2O_4$	279	*Small*, 2021, **17**, 2103501
Mo-Co_3O_4/CNTs	280	*Chemical Engineering Journal*, 2021, **408**, 127352
$NiCo_2O_3$@OMC	281	*Applied Catalysis B: Environmental*, 2019, **256**, 117852
$NiCo_2S_4$@NiFe LDH	287	*Applied Catalysis B: Environmental*, 2021, **286**, 119869
Fe_3O_4/Ni_3FeN	290	Small, 2020, **16**, 2002089
P-Co_3O_4	290	*Energy Environ. Sci.*, 2017, **10**, 2563-2569
L-Co_3O_4 NSs	290	*Nano Energy*, 2021, **83**, 105800
$CoWO_{4-x}$@C	295	*Applied Catalysis B: Environmental*, 2019, **259**, 118090
NF@$Co_{3-x}Ni_xO_4$	310	*Energy Storage Materials*, 2020, **24**, 272
ZIF-L-D-Co_3O_4/CC	310	*Adv. Sci.*, 2019, **6**, 1802243
Co_3O_{4-x}	330	*ACS Nano*, 2018, **12**, 8597-8605
ER-Co_3O_4 NWs-2	344	*ACS Energy Lett.*, 2019, **4**, 423-429
$NiCo_2O_4$/NCNTs/NiCo	350	*Chemical Engineering Journal*, 2021, **408**, 127814
LSM-20-Co	470	*Nano Energy*, 2020, **71**, 104564

Reference

1 G. Kresse and J. Furthmüller, *Phys. Rev. B*, 1996, **54**, 11169-11186.

2 P. E. Blochl, *Phys. Rev. B*, 1994, **50**, 17953-17979.

3 J. P. Perdew, K. Burke and M. Ernzerhof, *Phys. Rev. Lett.*, 1996, **77**, 3865-3868.

4 B. Hammer, L. B. Hansen and J. K. Nørskov, *Phys. Rev. B* 1999, **59**, 7413-7421.

5 H. J. Monkhorst and J. D. Pack, *Phys. Rev. B*, 1976, **13**, 5188-5192.

6 F. Calle-Vallejo, J. I. Martinez and J. Rossmeisl, *Phys. Chem. Chem. Phys.*, 2011, **13**, 15639-15643.

7 I. C. Man, H. Y. Su, F. Calle‐Vallejo, H. A. Hansen, J. I. Martínez, N. G. Inoglu, J. Kitchin, T. F. Jaramillo, J. K. Nørskov and J. Rossmeisl, *ChemCatChem*, 2011, **3**, 1159-1165.

8 X. Rong, J. Parolin and A. M. Kolpak, *ACS Catal.*, 2016, **6**, 1153-1158.

9 J. S. Yoo, Y. Liu, X. Rong and A. M. Kolpak, *J. Phys. Chem. Lett.*,, 2018, **9**, 1473-1479.

10 J. T. Mefford, X. Rong, A. M. Abakumov, W. G. Hardin, S. Dai, A. M. Kolpak, K. P. Johnston and K. J. Stevenson, *Nat. Commun.*, 2016, **7**, 11053.

11 Z.-F. Huang, J. Song, Y. Du, S. Xi, S. Dou, J. M. V. Nsanzimana, C. Wang, Z. J. Xu and X. Wang, *Nat. Energy*, 2019, **4**, 329-338.

12 G. Henkelman and H. Jónsson, *J. Chem. Phys.*, 2000, **113**, 9978-9985.

13 L. Jonas L. Haller, Michael J. Page, Stuart A. Macgregor, Mary F. Mahon and M. K. Whittlesey, *J. Am. Chem. Soc.*, 2009, **131**, 4604-4605.